Turbulent Mixing Variability in an Energetic Standing Meander of the Southern Ocean

AJITHA CYRIAC,[a,d] HELEN E. PHILLIPS,[a,b,c] NATHANIEL L. BINDOFF,[a,b,d,e] AND KURT POLZIN[f]

[a] *Institute for Marine and Antarctic Studies, University of Tasmania, Hobart, Tasmania, Australia*
[b] *Australian Antarctic Program Partnership, University of Tasmania, Hobart, Tasmania, Australia*
[c] *Australian Centre for Excellence in Antarctic Science, University of Tasmania, Hobart, Tasmania, Australia*
[d] *ARC Centre of Excellence in Climate Extremes, Hobart, Tasmania, Australia*
[e] *CSIRO Marine and Atmospheric Research, Hobart, Tasmania, Australia*
[f] *Department of Physical Oceanography, Woods Hole Oceanographic Institution, Woods Hole, Massachusetts*

(Manuscript received 26 August 2021, in final form 6 April 2022)

ABSTRACT: This study presents novel observational estimates of turbulent dissipation and mixing in a standing meander between the Southeast Indian Ridge and the Macquarie Ridge in the Southern Ocean. By applying a finescale parameterization on the temperature, salinity, and velocity profiles collected from Electromagnetic Autonomous Profiling Explorer (EM-APEX) floats in the upper 1600 m, we estimated the intensity and spatial distribution of dissipation rate and diapycnal mixing along the float tracks and investigated the sources. The indirect estimates indicate strong spatial and temporal variability of turbulent mixing varying from $O(10^{-6})$ to $O(10^{-3})$ m^2 s^{-1} in the upper 1600 m. Elevated turbulent mixing is mostly associated with the Subantarctic Front (SAF) and mesoscale eddies. In the upper 500 m, enhanced mixing is associated with downward-propagating wind-generated near-inertial waves as well as the interaction between cyclonic eddies and upward-propagating internal waves. In the study region, the local topography does not play a role in turbulent mixing in the upper part of the water column, which has similar values in profiles over rough and smooth topography. However, both remotely generated internal tides and lee waves could contribute to the upward-propagating energy. Our results point strongly to the generation of turbulent mixing through the interaction of internal waves and the intense mesoscale eddy field.

KEYWORDS: Diapycnal mixing; Eddies; Fronts; Inertia-gravity waves; Ocean dynamics

1. Introduction

The Antarctic Circumpolar Current (ACC) is the largest current in the world flowing from west to east around the continent of Antarctica unblocked by lateral boundaries. The complex topography along the path of the ACC consists of abyssal plains, rough midocean ridges and small-scale topographic features. These topographic features result in a nonuniform distribution of eddy kinetic energy (EKE) along the ACC with low EKE over flat abyssal plains and high EKE downstream of topography (Rintoul 2018). Recent studies have shown that many of the important physical processes relevant to the Southern Ocean dynamics are mainly focused in hotspot regions in the lee of topographic features. The instability of the current downstream of the topography results in the generation of standing meanders which are major generation sites for long-lived eddies (Frenger et al. 2015), where the cross frontal eddy heat fluxes are enhanced based on moored observations (Bryden and Heath 1985; Phillips and Rintoul 2000), sea surface height standard deviation (Foppert et al. 2017), and model simulations (e.g., Dufour et al. 2017). Moreover, the strong EKE in these regions leads to enhanced upwelling of Circumpolar Deep Water through along-isopycnal processes in the ACC interior (Tamsitt et al. 2017).

The topography upstream of ACC standing meanders promotes generation, propagation, and breaking of internal waves which contributes to turbulent mixing (Waterman et al. 2013; Meyer et al. 2016). Diapycnal mixing plays an important role in maintaining the ACC circulation by providing energy for upwelling and water mass transformation (Nikurashin et al. 2013). The intensity and distribution of diapycnal mixing is pivotal to the strength of the global overturning circulation (Polzin et al. 1997; Sloyan 2005). There is growing evidence from both observational (Sloyan 2005; Waterman et al. 2013; Sheen et al. 2013) and modeling studies (Nikurashin and Ferrari 2010; Nikurashin et al. 2013) that interaction of the ACC jets, mesoscale eddies and/or tides with rough topography results in bottom-generated internal waves. Observational studies show that elevated turbulence in the Southern Ocean is often associated with downward-propagating near-inertial waves in the upper 1–2 km and upward-propagating high-frequency waves 1–2 km above the ocean bottom (Waterman et al. 2013; Sheen et al. 2013; Meyer et al. 2015).

Here, we focus on the standing meander between the southeast Indian Ridge and Macquarie Ridge, south of Australia (Fig. 1). Macquarie Ridge is one of the major

Denotes content that is immediately available upon publication as open access.

Supplemental information related to this paper is available at the Journals Online website: https://doi.org/10.1175/JPO-D-21-0180.s1.

Corresponding author: Ajitha Cyriac, ajitha.cyriac@utas.edu.au

DOI: 10.1175/JPO-D-21-0180.1

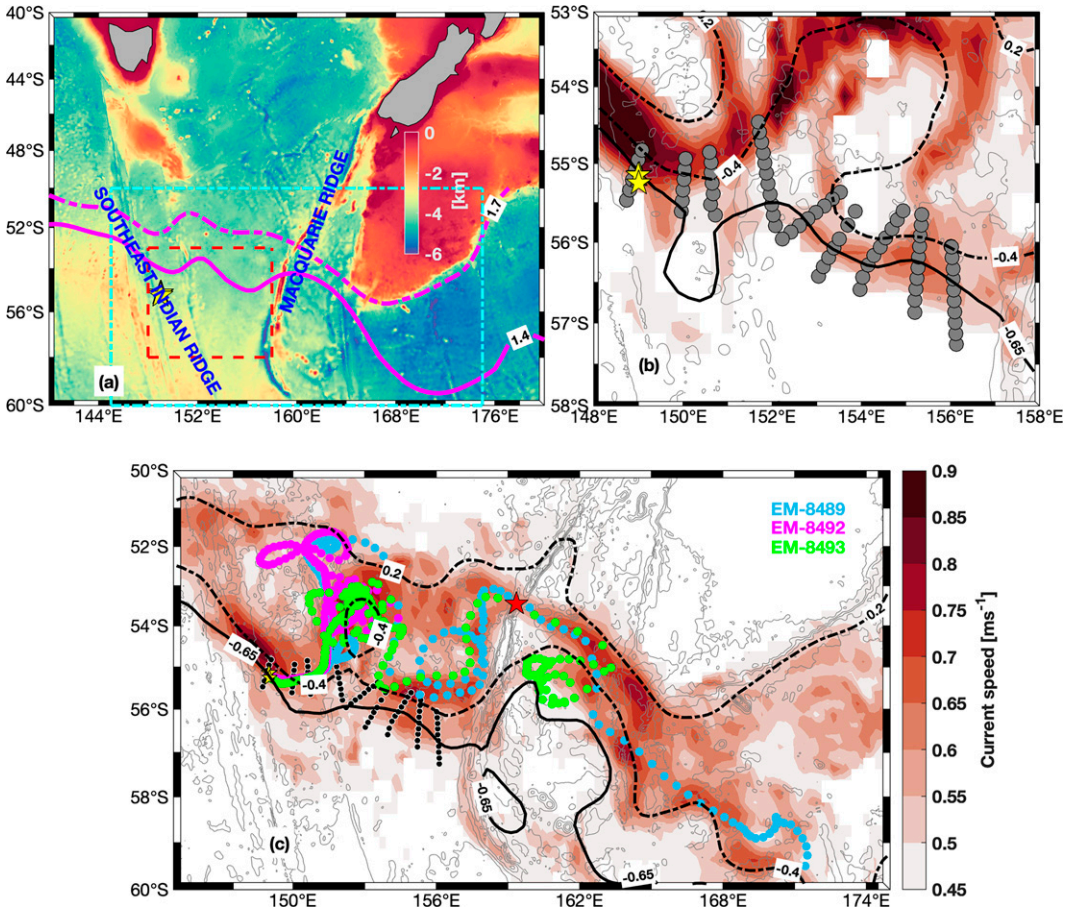

FIG. 1. (a) The bathymetry around the study region (color shading) where the ridge systems are marked. The thick and dashed magenta lines are the climatological dynamic height (0/2000 dbar) contours from CSIRO Atlas of Regional Oceans (CARS) for PF (1.4 m) and SAF (1.7 m) (Böning et al. 2008). The red dashed box and the cyan dashed box show the regions covered in (b) and (c), respectively. (b) The location of shipboard transects during DEFLECT across PF and SAF (gray circles). The yellow stars are the deployment locations of the EM-APEX floats used in this study. The background color shading is the average geostrophic current speed during the voyage. (c) The tracks of EM-8489 (blue), EM-8492 (magenta) and EM-8493 (green) are plotted over the mean geostrophic speed (shading) during the float sampling period from altimetry. Yellow stars represent the location of each float deployment. The shipboard stations of the voyage, as in (b), are marked as black circles. The red star at the ridge gap (53.45°S) shows the location of the current meter mooring mentioned in Fig. 8. In (b) and (c), gray contours are bathymetry at 1000, 2000, 3000, 4000, 5000, and 6000 m. The thick black line is the ADT contour of −0.65 m representing PF. The thick dashed ADT contours of 0.2 and −0.4 m represent the northern and southern branches of the SAF, respectively.

topographic obstacles for the ACC, extending from 47° to 58°S between Australia and New Zealand (Gordon 1975; Rintoul et al. 2014), with three deep, narrow gaps at 51°, 53.5°, and 56°S (Gordon 1978). A regional study at the Macquarie Ridge using MITgcm (Zhang and Nikurashin 2020) shows that the interaction of the eddies and fronts with the small-scale topography generates internal lee waves near the bottom. They found that the presence of small-scale topography is important in setting the curvature and location of the meander along with the vertical structure of the flow in the standing meander. The small-scale topography is associated with a significant reduction in EKE, which in turn raises questions of the role that eddy–internal wave conversions play in the response of the ACC to changing wind stress (Marshall et al. 2017). Moreover, Macquarie Ridge has been long identified as a region of strong barotropic to baroclinic M_2 tidal energy conversion in several global studies (Morozov 1995; Alford and Zhao 2007; Ansong et al. 2017; Nikurashin et al. 2013) and regional studies (Simmons et al. 2004; Waterhouse et al. 2018). The breaking of internal tides results in diapycnal mixing which plays a pivotal role in maintaining the meridional overturning circulation (e.g., Wunsch and Ferrari 2004). In addition, the strong and highly variable westerlies blowing over the meander near the ridge also makes it a region of strong wind energy input into near-inertial motions (Alford 2003; Whalen et al. 2018). It is thus reasonable to expect that the interactions between different processes such as strong mean current, mesoscale eddies,

tides, and internal waves contribute to the complex variability of turbulent mixing variability in the Macquarie Ridge region. However, the processes and energy pathways leading to turbulent mixing and its role in maintaining the large-scale circulation in this region have not been explored.

In this paper, we analyze the spatial and temporal variability of the turbulent mixing and investigate the responsible physical mechanisms using data from Electromagnetic Autonomous Profiling Explorer (EM-APEX) floats. The EM-APEX data were collected as part of the DEFLECT experiment, a comprehensive survey of the Polar Front (PF) standing meander that sits between the southeast Indian Ridge and the Macquarie Ridge near 150°E. The objective of DEFLECT was to explore the role of standing meanders in the momentum balance of the ACC. This experiment was motivated by the hypothesis that the flexing of standing meanders in response to accelerated flow upstream causes elevated dissipation of momentum through enhanced interfacial form stress and bottom drag (Thompson and Naveira Garabato 2014). This hypothesis is one of a collection of theories to explain the lack of increase in ACC transport in response to persistently increasing westerly winds over recent decades. Other theories include eddy saturation (Straub 1993; Hallberg and Gnanadesikan 2006), external forcing and intrinsic variability (Wilson et al. 2015), eddy damping (Marshall et al. 2017), and the development of an increased gyre circulation without affecting the circumpolar flow at the lee of the ridge (Nadeau and Ferrari 2015).

This paper is organized as follows. The study region, different datasets used in this study, and the details of the method of finescale parameterization used to estimate turbulent mixing from EM-APEX floats are explained in section 2. Section 3 describes the results of the study, including the regional ocean characteristics observed from the floats, the spatial and temporal variability of turbulent mixing estimates in the upper 1400 m, and the impact of different environmental factors such as wind, topography, and mesoscale vorticity. In section 4, we discuss the implications of mixing on regional water mass characteristics and different possible generation mechanisms for the internal waves. Section 5 provides a summary and conclusions of the study.

2. Data and methodology

a. Study region and experiment

The DEFLECT voyage data were collected at the standing meander of the PF at the Macquarie Ridge region over 54°–58°S, 148°–157°E, on voyage IN2018_V05 of the R/V *Investigator* from October to November 2018. The voyage survey consisted of 77 shipboard conductivity–temperature–depth/lowered acoustic Doppler current profiler (CTD/LADCP) stations, 47 vertical microstructure profiler (VMP) casts, eight cross-stream Triaxus transects, a tall mooring deployed at the crest of the meander, and a fleet of six EM-APEX floats and drifters deployed at the western edge of the meander. Data from the VMP and tall mooring were not available in time for this analysis and will be explored in future work. Of the six EM-APEX floats deployed, three of the floats are used in this study. Two out of three floats passed through the deep ridge gap at 53.5°S. These floats recorded temperature, salinity, and horizontal velocity components along the flow. The EM-APEX floats were deployed immediately following a CTD/LADCP cast, close to the mean position of the PF based on satellite sea surface height gradient and targeting the most recent position of the −0.65-cm absolute dynamic height contour on the day of the deployment. The shipboard hydrography and velocity data were used to calibrate the first few profiles of the float data. The floats followed the satellite derived streamlines of the PF for a few days before they were advected northward into a developing trough with intense eddy activity and a complicated interaction between the PF and the Subantarctic Front (SAF) (Fig. 1b). The float movement across the PF could be a response to a turning velocity vector with depth (Phillips and Bindoff 2014).

b. EM-APEX floats

The state of the art EM-APEX floats are enhanced Argo floats (Roemmich et al. 2004) which provide horizontal velocity data, in addition to temperature and salinity (Sanford et al. 2005). These floats estimate the horizontal velocity using the concept of motional induction in which an electromagnetic subsystem on the float measures the electrical potential difference generated when salty ocean water passes through the magnetic field of Earth. The floats provide high resolution vertical sampling and can be profiled rapidly to provide closely spaced profiles with which we can resolve different scales of motion such as internal waves (Meyer et al. 2016), turbulent mixing (Meyer et al. 2015; Cyriac et al. 2021), vertical structure of the frontal jets (Phillips and Bindoff 2014), and temperature and salinity filaments due to eddy stirring (H. E. Phillips et al. 2022, unpublished manuscript). More details of the float data quality control and data calibration can be found in Phillips and Bindoff (2014) and Cyriac et al. (2021).

The floats were deployed as pairs from different shipboard stations at the westernmost transect of the voyage (Fig. 1b). They were designed to continuously profile between the surface and ~1600 m until their batteries were expended. The temperature and salinity data have a vertical sampling spacing of 2–3 m and a mean horizontal spacing of 1–3 km whereas the horizontal velocity data have a vertical resolution of 3–4 m, capturing the internal wave scales. This profiling strategy allows the floats to resolve the inertial cycle (15.2-h period at 52°S) and provides six profiles per day on average. The floats switched to a "park and profile" mode before they passed through the ridge gap (around profile number 270). As a result, they only sent the up profiles disrupting the continuity of profiling (Fig. 2). In addition, two of the floats reduced their profile depths during this time resulting in shallower profiles in the second half of their float tracks (EM-8489 and EM-8493). Absolute velocity for this part of the float track (Fig. 2d) could not be estimated using only up profiles since this requires the up–down profile pairs of relative

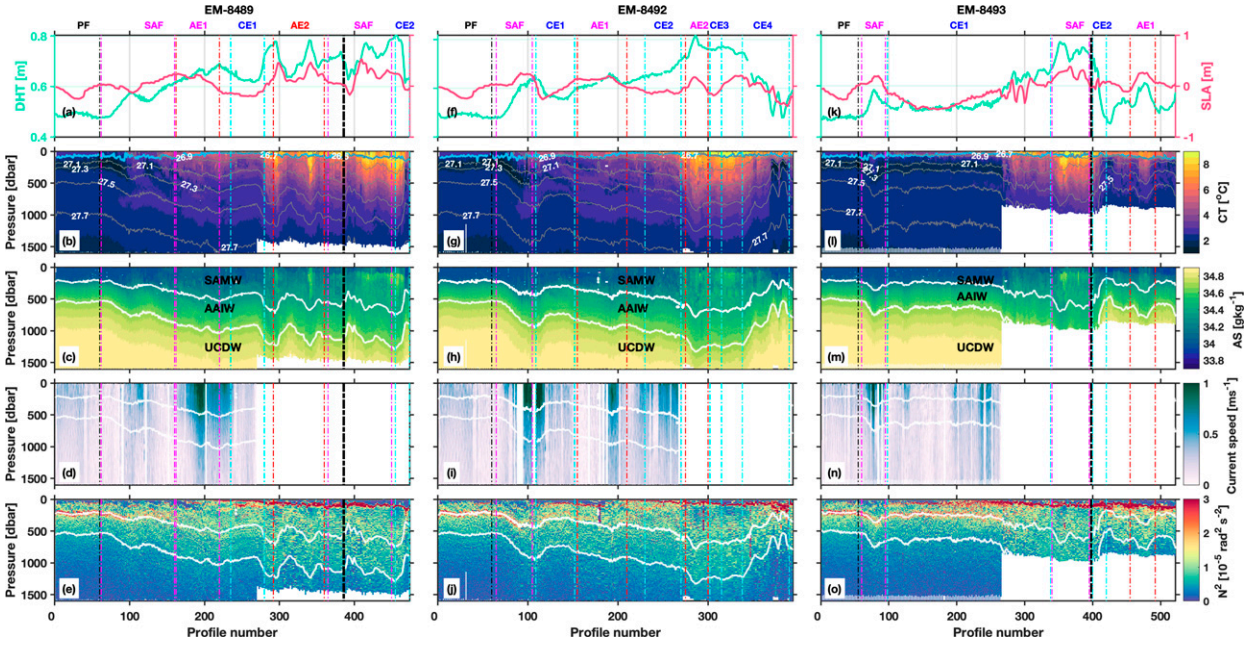

FIG. 2. The evolution of (a) DHT (100/800 dbar) (green) and SLA (red), (b) Conservative Temperature, (c) Absolute Salinity, (d) current speed, and (e) buoyancy frequency squared along the track of float EM-8489. (f)–(j) As in (a)–(d), but for float EM-8492. (k)–(o) As in (a)–(d), but for float EM-8493. The light gray lines on temperature plots are isopycnals with an interval of 0.2 kg m^{-3}. The evolution of the mixed layer depth along each float track is also marked (blue line). The thick white lines on salinity are different water masses defined as $\sigma_\theta \leq 27.2$ kg m^{-3} for SAMW, 27.2 kg m^{-3} $\leq \sigma_\theta \leq$ 27.53 kg m^{-3} for AAIW, and 27.53 kg m^{-3} $\leq \sigma_\theta \leq$ 27.8 kg m^{-3} for UCDW. The current speed in the second half of the float track in all the floats is missing due to the lack of absolute velocities (section 3a). Note that the temperature, salinity, and buoyancy frequency after profile number ~270 in all floats consists of up profiles only. The vertical black dashed line shows the location of each float track where it crossed the Macquarie Ridge. The vertical colored lines represent different dynamic regions that each float profiled. The thin black vertical dashed lines show the end of PF in each float track whereas the magenta lines show the profiles in the SAF. The cyan (red) lines represent regions of cyclonic (anticyclonic) eddies along the float tracks. Each of these regions are marked on the top panels of each float. Note that the numbering of the eddies is independent for each float.

velocity between the two GPS surface positions of both up and down profiles to estimate the depth-independent reference velocity (Phillips and Bindoff 2014).

c. *Finescale parameterization*

The dissipation rate of turbulent kinetic energy (ε) can be estimated indirectly from finescale measurements of shear (vertical gradient of horizontal velocity) and strain (vertical gradient of vertical isopycnal displacement) using wave–wave interaction parameterizations (Henyey et al. 1986; Gregg et al. 2003; Polzin et al. 2014). This method is based on the assumption of energy cascade between internal wave scales to dissipative scales in the ocean due to nonlinear interactions of internal waves. Here, we integrate the shear variance spectra between 383 m and a cutoff wavenumber m_c, where m_c is the wavenumber at which the integrated shear variance reaches $2\pi N^2/10$ or 30 m, whichever is larger. We set the high wavenumber limit of the strain variance spectrum to be equal to the limit identified in the corresponding shear spectrum of each profile to avoid integrating into the instrument noise of the strain spectrum (Cyriac et al. 2021). However, we find that the patterns of mixing estimates are generally robust to the changes in integration limits. We further limited our integration between the base of the mixed layer and 1600 m to avoid high strain variance in the mixed layer which are not necessarily due to internal waves. The dissipation rate of turbulent kinetic energy can be written as (Gregg 1989; Polzin et al. 1995; Garabato et al. 2004; Meyer et al. 2015)

$$\varepsilon = \varepsilon_0 \left(\frac{N^2}{N_0^2}\right) \frac{\langle V_z^2 \rangle^2}{\langle V_{z-\mathrm{GM}}^2 \rangle^2} h(R_\omega) L(f, N), \tag{1}$$

where

$$h(R_\omega) = \frac{3(R_\omega + 1)}{2R_\omega \sqrt{2(R_\omega - 1)}}, \text{ and} \tag{2}$$

$$L(f, N) = \left(\frac{f}{f_0}\right) \frac{\cosh^{-1}(N/f)}{\cosh^{-1}(N_0/f_0)}. \tag{3}$$

Here, $\varepsilon_0 = 8 \times 10^{-10}$ W kg^{-1}, $N_0 = 3$ cph, $f_0 = 7.836 \times 10^{-5}$ s^{-1}, N is the local buoyancy frequency, and f is the local Coriolis frequency. Here $\langle V_z^2 \rangle$ is the vertical shear variance normalized by N and $\langle V_{z-\mathrm{GM}}^2 \rangle$ is the corresponding shear variance predicted by the Garrett–Munk (GM76) model. The angle brackets denote the wavenumber range over which the shear and strain variances are integrated. The range of integration varies from minimum wavenumber to a cutoff value (Fig. S1) above

which the nonlinear effects lead to wave breaking (Polzin et al. 2014). Here, $h(R_\omega)$ accounts for the dominant frequency in the observed wave field and $L(f, N)$ contains the latitudinal dependence (Gregg et al. 2003).

The finescale parameterization also provides information about the frequency content of the waves and their direction of propagation. The bulk frequency content of the internal wave field can be estimated from the shear–strain variance ratio (R_ω) as

$$R_\omega = \frac{\langle V_z^2 \rangle}{\langle \xi_z^2 \rangle}, \tag{4}$$

where $\langle V_z^2 \rangle$ is the vertical shear variance normalized by N. Here, ξ_z is the strain derived as $\xi_z = (N^2 - [N_{\text{ref}}^2])/[N_{\text{ref}}^2]$, where $[N_{\text{ref}}^2]$ is the mean squared buoyancy frequency. The local buoyancy frequency, $N^2 = -(g/\rho_0)(\partial\rho_\theta/\partial z)$, is estimated using the adiabatic levelling method (Bray and Fofonoff 1981), where ρ_θ is the potential density estimated from the EM-APEX float profiles. The $[N_{\text{ref}}^2]$ is calculated as a moving average of 20 consecutive profiles of buoyancy frequency estimated over a longer pressure window of 24 m, and square brackets represent the horizontal averaging.

Low values of R_ω suggest the presence of high-frequency waves whereas large values of R_ω indicates the dominance of near-inertial frequencies. Under the single wave approximation, the intrinsic frequency of the wave can be written as $\omega = f\sqrt{(R_\omega + 1)/(R_\omega - 1)}$, where f is the inertial frequency (Polzin et al. 1995). The dominant direction of propagation of the internal waves can be estimated from the ratio of counterclockwise (CCW) to clockwise (CW) shear variance (polarization ratio). Polarization ratio larger than one suggests a dominance of downward (upward) energy propagation in the southern (northern) hemisphere.

The diapycnal turbulent eddy diffusivity (K_ρ), and hereinafter referred to as diffusivity, can be estimated from ε using the Osborn (1980) relation, $K_\rho = \Gamma\varepsilon/N^2$. Here, Γ is the dissipation ratio or mixing efficiency, taken as a constant of 0.2 (Gregg et al. 2018), and N is the buoyancy frequency.

d. Mixed layer depth, dynamic height, relative vorticity, and bathymetry

The mixed layer depth (MLD) is defined as the depth at which the potential density changes by 0.03 kg m^{-3} from the value at 10 m (de Boyer Montégut et al. 2004). The dynamic height (DHT) along the float tracks is calculated relative to 800 dbar, a depth range common to all profiles (Figs. 2a,f,k). The vertical component of the relative vorticity (ζ) is estimated as $\zeta = (\partial v/\partial x) - (\partial u/\partial y)$, where u (v) is the daily surface geostrophic eastward (northward) velocity component obtained from satellite altimetry. Negative (positive) values of relative vorticity have similar (opposite) sign as the planetary vorticity and are referred to as cyclonic (anticyclonic). The daily sea level anomaly (SLA) and absolute surface geostrophic velocities were obtained from Copernicus Marine Environment Monitoring Service (CMEMS) on a 0.25° × 0.25° spatial grid (https://marine.copernicus.eu/). We further interpolated the relative vorticity, along with absolute dynamic topography (ADT) and geostrophic velocity from altimetry into the time and location of the float profiles. The General Bathymetric Chart of the Oceans (GEBCO) topography data with a 30-arc-s grid are used to contour bathymetry (https://www.gebco.net/).

3. Regional ocean dynamics

a. ACC fronts and water masses

ACC fronts around Antarctica have been defined in previous studies based on subsurface water properties from hydrographic data (Orsi et al. 1995) and sea surface height maps from altimetry data (Sokolov and Rintoul 2007, 2009). Here, we define the fronts based on the altimetry values of absolute dynamic topography, where ADT values of −0.65 m define the mean PF, −0.4 m define the southern branch of the SAF, and 0.2 m define the northern branch of the SAF (Sokolov and Rintoul 2009; Patel et al. 2019). We identify the location of eddies using animations of daily SLA maps from CMEMS (see the online supplemental material). We further sort the float profiles into regions of fronts and mesoscale eddies based on SLA contours and their position relative to the ADT values in the animations, relative vorticity from sea surface geostrophic velocity computed from ADT, dynamic height of the 100-dbar surface relative to 800 dbar, T–S characteristics, and velocity data from the floats. The floats are either within the PF or SAF or in mesoscale eddies. Due to the richness of the mesoscale eddies during the float profiling, the profiles are assigned to eddies either if the float loops around the eddy or if there is a strong imprint in the profiles when the float passed through an eddy periphery (e.g., AE1 in float EM-8489). The rest of the profiles are assigned to either the PF or the SAF. A total of 89% of profiles are assigned to eddies (cyclonic, 35%, anticyclonic, 18%) or the PF (13%) or the SAF (23%).

The different ACC fronts and major water masses can be identified from the temperature, salinity, and velocity data along the float tracks. The PF is traditionally defined as the northernmost extent of a temperature minimum layer of 2°C at a depth of 200 m (Orsi et al. 1995). This subsurface temperature minimum layer is seen at the beginning of all float tracks (Figs. 2b,g,l) and also in the cyclonic eddy pinched off from the SAF (CE1 in EM-8493). The isopycnals are flat in this part of the tracks with uniform salinity distribution across profiles (Figs. 2c,h,m). The mean surface current speed in the PF is moderate (0.18 m s^{-1}) with a mean mixed layer depth of 76 m (Figs. 2d,i,n). The sudden descent of isopycnals and higher current speeds (>1 m s^{-1}) immediately after the subsurface temperature minimum marks the beginning of the SAF in the float tracks. The southern (sSAF) can also be identified from the temperature criterion of 4°–6°C at a depth range of 300–400 m (Sokolov and Rintoul 2002).

We also identify the major water masses in the region from the float data. The Subantarctic Mode Water (SAMW) is identified as the layer with potential density $\sigma_\theta \leq 27.2$ kg m^{-3}. The salinity signature of SAMW is clearer in the northernmost profiles of the floats (Figs. 2c,h,m). The Antarctic Intermediate

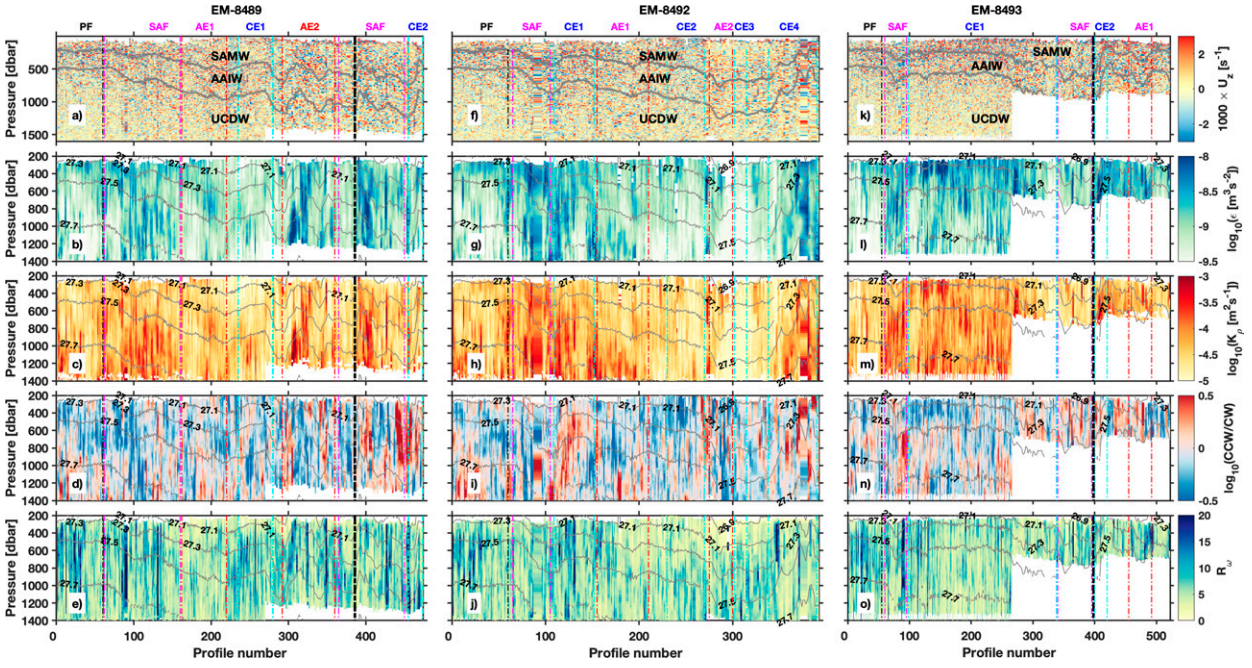

FIG. 3. As in Fig. 2, but for (a) vertical shear, (b) dissipation rate, (c) diffusivity, (d) polarization ratio, and (e) shear-strain ratio along the track of float EM-8489. (f)–(j) As in (a)–(d), but for float EM-8492. (k)–(o) As in (a)–(d), but for float EM-8493. Note that the all the mixing estimates after profile number ~270 in all floats consists of up profiles only.

Water (AAIW) is defined as $27.2 \leq \sigma_\theta \leq 27.53$ kg m^{-3} with a low-salinity tongue. The Upper Circumpolar Deep Water (UCDW) is identified as $27.53 \leq \sigma_\theta \leq 27.8$ kg m^{-3} with Absolute Salinity values larger than 34.5 g kg^{-1} in the float profiles.

b. *Float observations*

A detailed picture of the temperature, salinity and velocity fields of fronts and mesoscale eddies as observed by the floats along their trajectories in the upper 1600 m is given in Fig. 2. Note that in Figs. 2 and 3, the profiles after profile number ~270 include only up profiles since absolute velocity (and speed) cannot be calculated from the relative velocity. After their deployment, the floats traveled together along streamlines of the PF estimated from the satellite derived ADT for a few days and then entered into the SAF (Figs. 2 and 1c). Between the northern (nSAF) and sSAF branches of the SAF, the floats followed different paths and looped around energetic mesoscale eddies. The signatures of fronts and mesoscale eddies can be identified from both altimetry and the dynamic height derived from the float temperature and salinity measurements (Fig. 2a). After the float deployments, a cyclonic eddy was formed downstream, which can be identified as a meander-like structure pinching off from the sSAF (Figs. 1b,c). Of the three floats, two were advected eastward along the SAF and passed through the 53.3°S gap of the ridge, through which a large portion of the ACC passes (Rintoul et al. 2014).

Float EM-8489 had the longest trajectory covering ~20° of longitude between October 2018 and April 2019. After entering the SAF, float EM-8489 profiled along the edges of several mesoscale eddies (Figs. 2a–e). It looped around an anticyclonic eddy (AE2) before entering the ridge gap. Downstream of the ridge, the float profiled along the sSAF streamlines and occasionally along the edges of mesoscale eddies before its battery died. Float EM-8492 had the shortest track between October 2018 and February 2019 during which the float covered ~5° of longitude between the northern and southern branches of SAF (Figs. 2f–j). It profiled along the edges of several eddies before looping around the PF cyclonic eddy and died. Float EM-8493 had a similar trajectory as that of the float EM-8489 (Fig. 1c). EM-8493 had the longest lifespan (October 2018–May 2019) and covered ~12° of longitude during that time (Figs. 2k–o). It profiled around the PF cyclonic eddy for a major part of its track before crossing the ridge through the 53.3°S gap. Downstream of the ridge, EM-8493 profiled through the edges of a cyclonic and anticyclonic eddy pair (CE2 and AE1 in EM-8493) before its battery died.

4. Turbulent mixing variability

The distribution of vertical shear, dissipation rate (ε), diapycnal diffusivity (K_ρ), polarization ratio (CCW/CW), and shear–strain variance ratio (R_ω) along the float tracks is shown in Fig. 3. The estimates of dissipation rate (Figs. 3b,g,l) and diffusivity (Figs. 3c,h,m) show strong variability with depth along the float tracks. We think of the variability along the float tracks as primarily being due to spatial variations. However, since the floats profiled for about 6 months, it is possible that there is a contribution from temporal variability in the mixing estimates (Whalen et al. 2018). Overall, the dissipation rate and diffusivity estimates are enhanced in

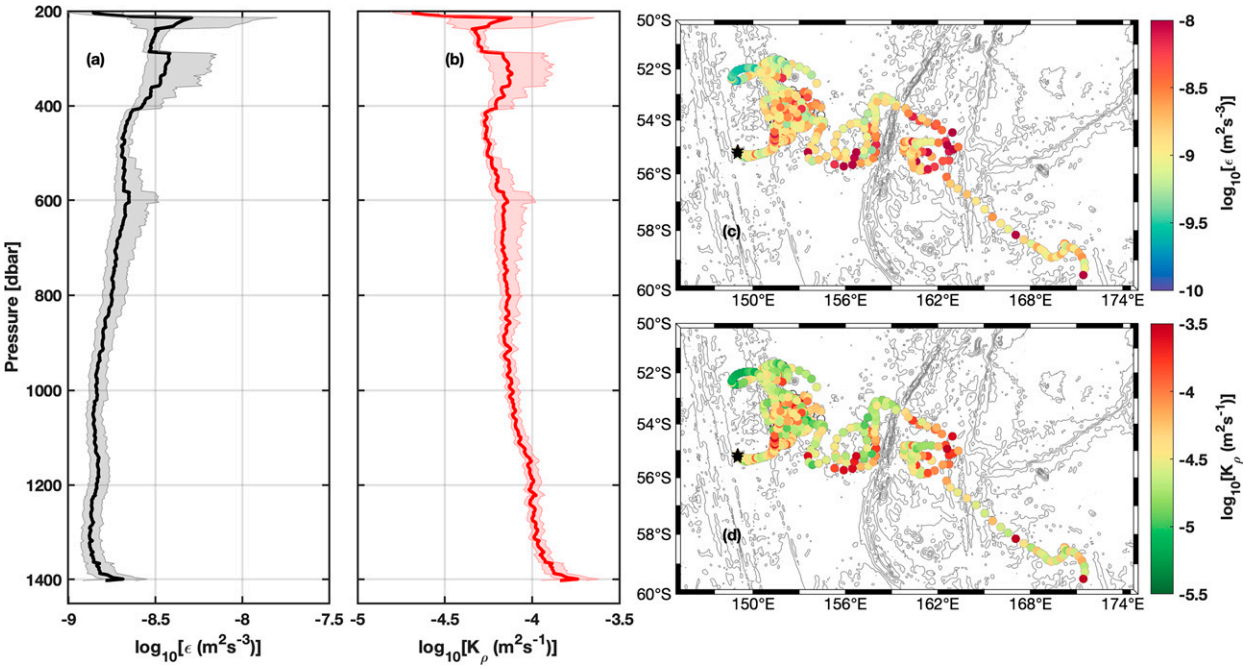

FIG. 4. Mean vertical profiles of (a) dissipation rate and (b) diffusivity. Shaded areas show 90% confidence intervals estimated from bootstrap sampling. Distribution of depth averaged values of (c) dissipation rate and (d) diffusivity along the float tracks with bathymetry contours at the same intervals as in Fig. 2 in gray. The deployment location of each float is marked as a black star near 150°E.

regions of the SAF and mesoscale eddies relative to background conditions. The float estimates have a mean dissipation rate of $2.14 \pm 1.4 \times 10^{-9}$ m^2 s^{-3} and a mean diffusivity of $7.7 \pm 1.2 \times 10^{-5}$ m^2 s^{-1} (calculated as $\langle \Gamma([\varepsilon]/[N^2]) \rangle$, where square brackets represent horizontal averaging and angle brackets represent vertical averaging) in the upper 1400 m of the Macquarie Ridge region. Here, and in the following estimates, errors represent standard errors. These standard errors assume that each profile is independent (about 1300) and that there is a vertical correlation of the noise of about 30 m (i.e., every 10 bins). From previous studies, there is a factor of 3 uncertainty in inferring dissipation rate and diffusivity using finescale parameterization (Polzin et al. 2002).

Although the polarization ratio (Figs. 3d,i,n) and R_ω (Figs. 3e,j,o) along the float tracks are rather variable, we can identify some patterns. The polarization ratio estimates suggest that there are approximately equal amounts of upward (negative $\log_{10}$[CCW/CW]) and downward-propagating energy in the upper 1400 m in this region. There is evidence of strong downward propagation in regions of the PF (e.g., profiles 10–30 in EM-8489), cyclonic eddies (e.g., profiles 120–130 in EM-8492), SAF (e.g., profiles 80–100 in EM-8493), and anticyclonic eddies (e.g., profiles 470–480 in EM-8493) throughout the water column. There are also strong signals of upward propagation in the upper 500 m especially in cyclonic eddies (e.g., CE1 in EM-8493). From the large values of R_ω, we see that the PF (and often SAF) is mostly characterized by low-frequency near-inertial waves in all the floats (e.g., profiles from 10 to 30 in EM-8489). Higher-frequency waves are characterized by smaller values of R_ω. There is also evidence of near-inertial waves in other dynamic regions at different depths. However, the pattern is not as consistent as that in the PF across all floats. The floats have a mean polarization ratio of 1.06 ± 0.001 and R_ω of 6.35 ± 0.002. Both are calculated as the mean of all profiles presented in Fig. 3, including the shallow profiles of EM-8493.

The mean vertical profile of dissipation rate (Fig. 4a) slightly decreases with depth, whereas the mean diffusivity profile (Fig. 4b) slightly increases with depth. Depth-averaged values of dissipation rate and diffusivity in the upper 200–1400 m for individual profiles are shown in Figs. 4c and 4d. They are highly spatially variable with elevated values mostly associated with loops around mesoscale eddies (Figs. 4c,d) with peak values reaching 1.45×10^{-7} m^2 s^{-3} and 3×10^{-3} m^2 s^{-1} for dissipation and diffusivity, respectively. The profiles in the SAF at the beginning of the float tracks also show enhanced dissipation even though they are not as high as in the eddies downstream of the Macquarie Ridge. Note that the profiles from EM-8493 east of 154°E, after around profile 270, only allow estimates to 600-m depth (Figs. 2 and 3).

The floats profiled most of the time between the northern and southern branches of the SAF with some early profiles in the PF soon after deployment (Fig. 1c). Here, we further examine the mean profiles of mixing estimates in the PF (13% of profiles) and SAF (23% of profiles, Figs. 5a–d). The dissipation rate and diffusivity estimates are higher in the SAF than in the PF. In the upper 800 m, the mean vertical distribution of polarization ratio shows downward propagation in the SAF [$\log_{10}$(CCW/CW) values larger than 0], whereas upward

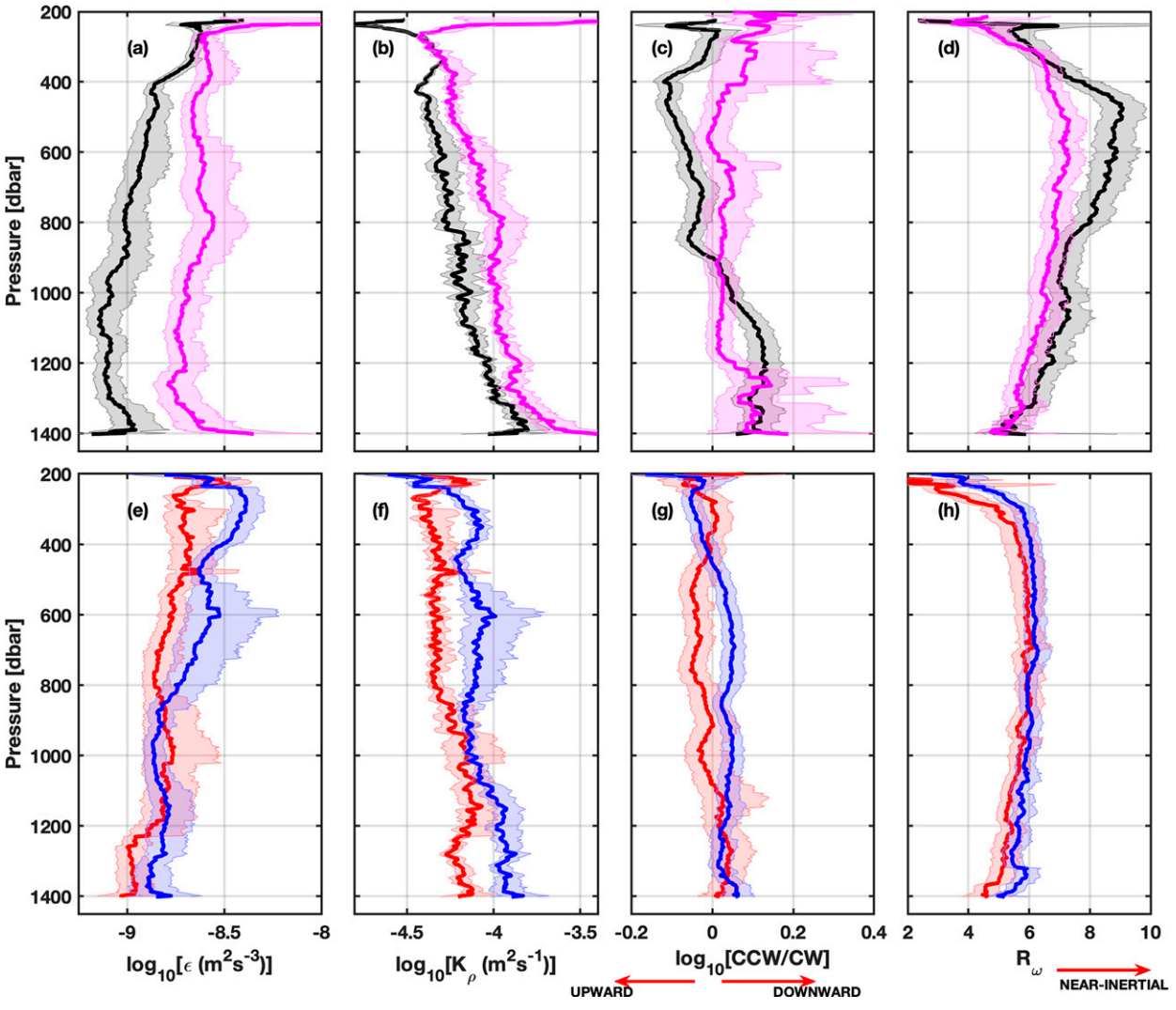

FIG. 5. Mean vertical profiles of (a),(e) dissipation rate; (b),(f) diffusivity; (c),(g) polarization ratio; and (d),(h) shear–strain ratio in regions of PF (black), SAF (pink), cyclonic (blue), and anticyclonic (red) eddies. In (c) and (g), positive (negative) values represent downward energy propagation. Shaded areas in all panels show 90% confidence intervals estimated from bootstrap sampling.

propagation in the PF (Fig. 5c). Below 1000 m, both regions show downward propagation. On the other hand, the R_ω values in the PF are higher than those in the SAF at all depths suggesting a stronger influence of near-inertial waves in the mixing distribution within the PF. The R_ω is highest in the depth range 400–800 m in the PF (Fig. 5d). The upward propagation of near-inertial waves in the PF is quite fascinating as it suggests the possibility of spontaneous generation of near-inertial waves during geostrophic adjustment of the front (e.g., Vanneste 2013). This possibility will be explored further using cross frontal measurements of shear from the shipboard data in a future study.

The floats encountered numerous mesoscale eddies since they were deployed in a region of strong EKE. The mean profiles of dissipation rate and diffusivity are slightly enhanced in cyclonic eddies in the upper 800 m compared to the anticyclonic eddies (Figs. 5e,f). The mean polarization ratio shows downward propagation ($\log_{10}$[CCW/CW] values larger than 0) in the cyclonic eddies with upward propagation in anticyclonic eddies between 400 and 1100 m (Fig. 5g). There is not much difference in R_ω values between cyclonic and anticyclonic eddies (Fig. 5e). Both show a tendency for high-frequency waves above 300 m, with a mean R_ω of approximately 6 (~1.18f) through most of the water column.

The mean values of mixing estimates in different dynamic regions are given in Table 1. Overall, the mean dissipation rate is highest in cyclonic eddies and lowest in the PF. The highest mixing is in the SAF, and the weakest is in anticyclonic eddies. The mean direction of propagation is downward (polarization ratio > 1) in all regions except in anticyclonic eddies (0.99). The PF has the highest value of R_ω with similar values in eddy regions irrespective of the sign of their vorticity (Table 1, Fig. 5e). This suggests that the PF has more near-inertial frequency waves than the other regions.

TABLE 1. Mean values of mixing estimates in different dynamic regions between 200 and 1400 m. Errors represent the standard error in the mean. The standard errors on these estimates assume each profile is independent in each dynamic region and that there is a vertical correlation of the noise of about 30 m (i.e., every 10 bins).

Parameter	PF	SAF	CE	AE
ε ($\times 10^{-10}$ m^2 s^{-3})	11.5 ± 1.4	23.0 ± 5.4	23.2 ± 7.5	17.8 ± 3.3
K_ρ ($\times 10^{-5}$ m^2 s^{-1})	6.5 ± 0.4	10.8 ± 1.4	8.4 ± 0.3	5.6 ± 0.2
Polarization ratio	1.0 ± 0.04	1.2 ± 0.2	1.1 ± 0.05	1.0 ± 0.06
R_ω	7.4 ± 0.2	6.6 ± 0.2	5.8 ± 0.2	5.9 ± 0.2

5. Factors modulating turbulence

There are several possible parameters that can contribute to the observed mixing variations in the Macquarie Ridge region: the presence of strong mesoscale variability, varying topography, strong wind forcing, and the rapidly merging and splitting ACC jets. Here we investigate the role of each of these factors, if any, in controlling the turbulent mixing variability in this region.

a. *Wind*

Wind energy is one of the major sources of power for turbulent mixing in the ocean interior (Wunsch and Ferrari 2004). The storms and strong wind events generate time-varying wind stress which perturbs the base of the mixed layer at near-inertial frequency. These oscillations transfer energy into near-inertial internal waves that propagate into the ocean interior (Alford et al. 2016) and contribute to turbulent mixing (Alford et al. 2012). Global studies show that the Macquarie Ridge region has strong wind energy input into near-inertial motions in the mixed layer (e.g., Alford 2003; Whalen et al. 2018) due to the presence of strong westerly winds. Here we analyze the role of wind forcing in the observed mixing estimates in the upper 500 m of the water column.

A mixed layer slab model without mesoscale currents is used to estimate the wind energy flux input into near-inertial motions in the mixed layer (Pollard and Millard 1970). Details of the model are described in the appendix. This energy flux is then averaged over a period of 15–20 days prior to each mixing estimate from the float profiles to account for the time taken for a near-inertial wave with a vertical group velocity of ~20 m day^{-1} (e.g., Alford et al. 2012) to reach 400 m. In Fig. 6 we test the response of dissipation rate (diffusivity) in the upper

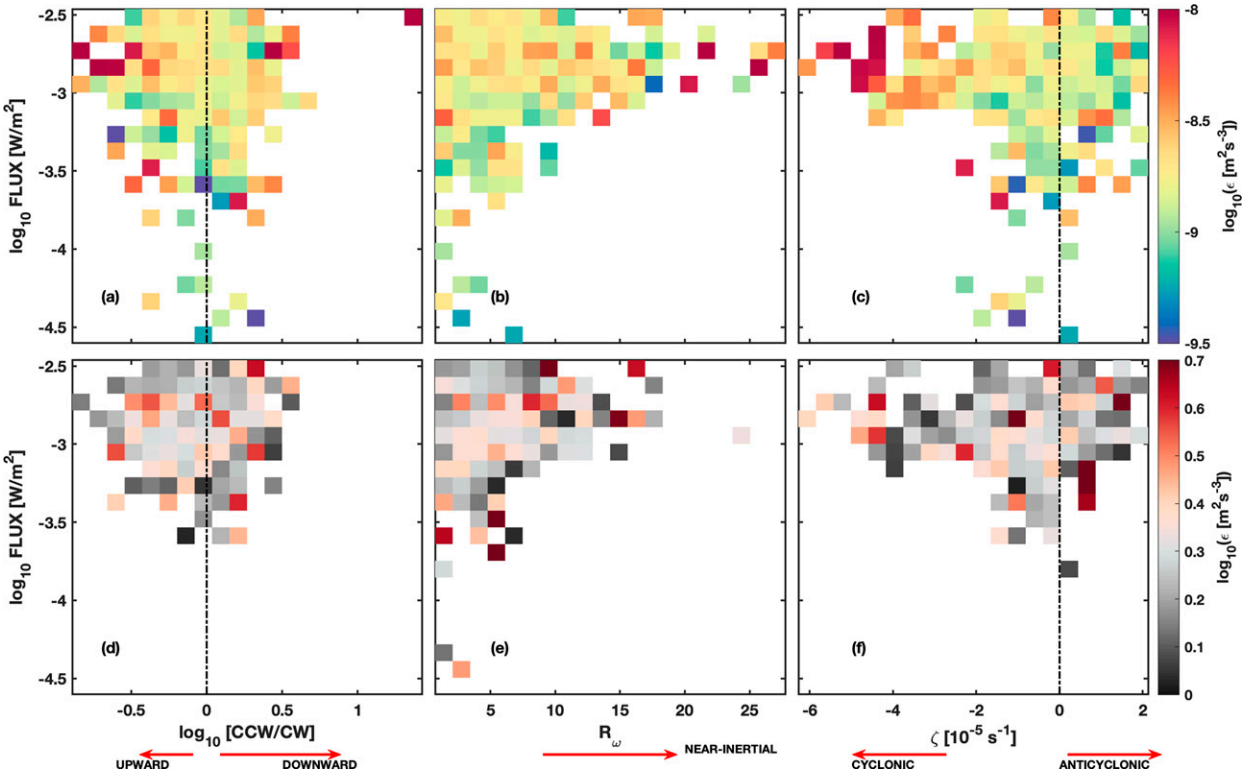

FIG. 6. Mean dissipation rate in the upper 400 m as a function of wind flux and (a) polarization ratio, (b) R_ω, and (c) relative vorticity and (d)–(f) the corresponding standard deviations. The vertical dashed lines in (a) and (d) separate regions of upward energy propagation (CCW/CW < 1) and downward energy propagation (CCW/CW > 1). The black vertical dashed line in (c) and (f) marks when $\zeta = 0$, separating cyclonic (negative values) and anticyclonic (positive values) vorticity.

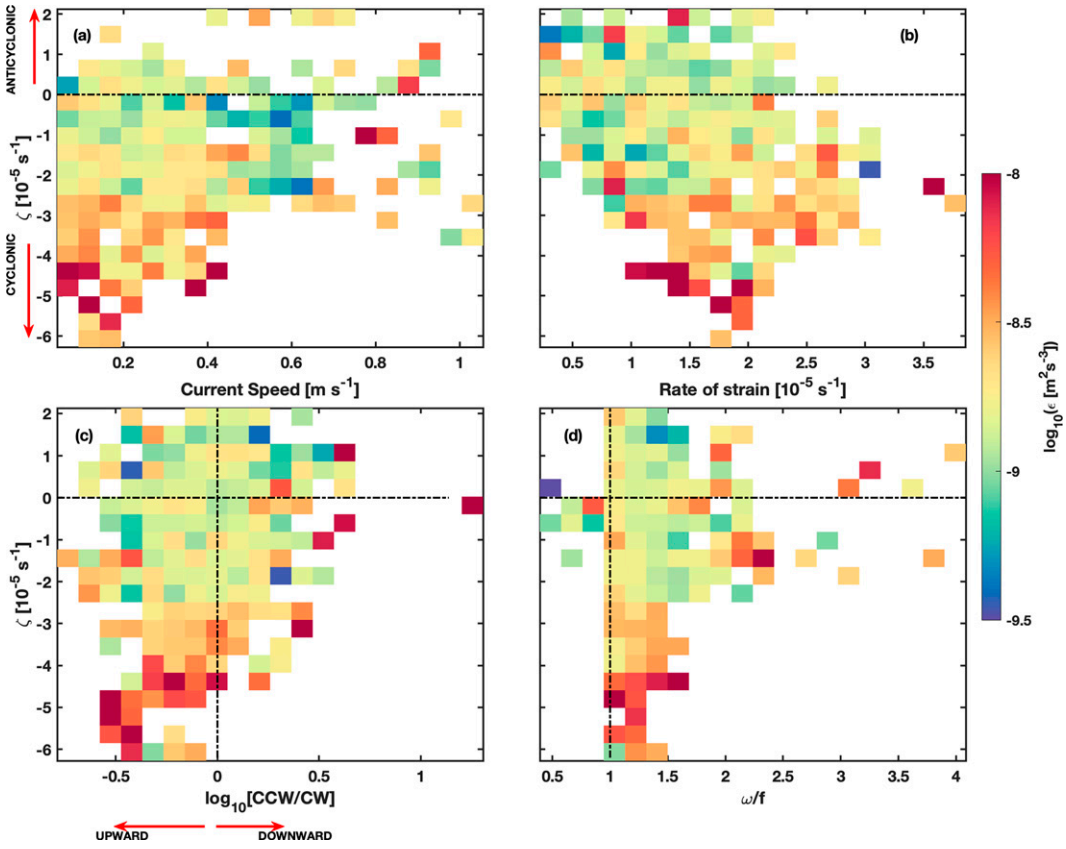

FIG. 7. Depth averaged values of dissipation rate as a function of relative vorticity and (a) current speed, (b) rate of strain, (c) polarization ratio, and (d) wave frequency content between 200 and 500 m. The black horizontal dashed line in all panels marks when $\zeta = 0$, separating cyclonic (negative values) and anticyclonic vorticity (positive values). The vertical dashed line in panel (c) separates regions of upward energy propagation (negative values) and downward energy propagation (positive values). The vertical dashed line in (d) marks the region when $\omega = f$.

400 m to the time-averaged wind energy flux with diagnostic parameters such as polarization ratio, R_ω and relative vorticity.

Elevated dissipation rates (diffusivity) in the upper 400 m are found to be associated with increased wind energy flux *and* both downward and upward energy propagation (Fig. 6a). Further, the dissipation rate is elevated for higher values of R_ω suggesting a dominant role of near-inertial waves (Fig. 6b). The interpretation of these patterns is not straightforward. The predominance of downward energy propagation and near-inertial frequency content in the upper water column is consistent with wind-generated near-inertial waves propagating downward from the base of the mixed layer into the ocean interior.

Previous studies suggest that regions of anticyclonic vorticity are effective in draining near-inertial energy from the surface into the ocean interior followed by subsequent trapping of surface generated near-inertial waves and thereby elevating turbulent mixing (Kunze 1985). The relationship with relative vorticity is shown in Fig. 6c. Dissipation rate (diffusivity) associated with anticyclonic vorticity ($\zeta > 0$) in high wind energy flux conditions is weak to moderate in the upper water column whereas the dissipation rate is enhanced in the presence of cyclonic vorticity. Thus, even though there is dominant downward propagation of near-inertial waves, the impact of anticyclonic vorticity in draining near-inertial energy leading to dissipation is less evident from the float data. This could be due to the coarse resolution of the altimetry data compared to the high-resolution float data from the ocean interior.

b. *Mesoscale vorticity*

Previous studies suggest that the mesoscale environment can modulate the turbulent mixing variability in the global ocean through interactions with near-inertial waves (e.g., Kunze 1985; Polzin 2008) and internal tides (e.g., Chavanne et al. 2010). Using strain information from Argo floats, Whalen et al. (2012) show that the regions of high EKE are associated with regions of high dissipation rate and elevated diffusivity in high latitudes. Thus, it is very likely that the strong eddy field in our study region is a strong contributor to the observed mixing estimates. Here, we investigate the role of mesoscale vorticity in the observed mixing variability by analyzing the relation between current speed, polarization ratio and shear–strain ratio in the upper 500 m.

We found that the dissipation rate (diffusivity) increases with an increase in cyclonic vorticity (Fig. 7). However, in the upper 500 m, we do not see a significant correlation between

depth averaged dissipation rate (diffusivity) and current speed (Fig. 7a). Higher current speed is an indication of the presence of fronts and mesoscale eddies, which can interact with the bottom topography to generate internal waves and mixing in the ACC. The elevated dissipation rate is more associated with weak to moderate current speeds. Further, the correlation between current speed and dissipation rate in the deeper part of the dataset (1200–1400 m) is also weak (0.15, not shown). This suggests that the high current speed associated with fronts and eddies may not contribute to the observed mixing pattern in the upper water column of the study region. Similarly, we investigated the role of rate of strain [$\sqrt{(S_n^2 + S_s^2)}$, where $S_n = U_x - V_y$ is the normal component and $S_s = U_y + V_x$ is the shear component of the background strain field; the subscripts represent the spatial derivatives] in the observed mixing variability. If the rate of strain of an eddy field exceeds relative vorticity, the amplitude of the internal wave grows exponentially, leading to dissipation of the wave (Bühler and McIntyre 2005; Polzin 2008). We found that the dissipation rate has greater variations associated with relative vorticity than rate of strain (Fig. 7b). This suggests that the enhanced dissipation rate in cyclonic eddies is associated with the relative vorticity of the eddy than the eddy strain field.

Using observations of semidiurnal surface tidal currents, Chavanne et al. (2010) shows that the cyclonic eddies can modulate the vertical propagation of internal tides and further trigger turbulent mixing near the surface. We investigate the role of this mechanism by analyzing the dominant direction of propagation of the internal waves associated with strong cyclonic vorticity through the polarization ratio (Fig. 7b). We find that the elevated dissipation rate is associated with upward-propagating internal waves in cyclonic vorticity in the upper 500 m. We further looked at the frequency content of the waves using R_ω. The elevated dissipation rate in the cyclonic vorticity is associated with internal waves of frequency $f - 1.7f$ (Fig. 7c), where the semidiurnal tidal frequency at 54°S is ~1.2f. It is therefore likely that the main mechanism of elevated turbulent dissipation in the upper water column in this region is the interaction between cyclonic eddies and upward-propagating internal tides at semidiurnal frequency, with a small contribution from higher-frequency waves.

c. Topography

Topography plays an important role in the turbulent mixing variability of the Southern Ocean. Mixing is enhanced over rough topography where internal lee waves generated from the interactions between geostrophic flow with rough topography propagate upward and break (Nikurashin and Ferrari 2010; Waterman et al. 2013; Sheen et al. 2013). Away from the sea surface and bottom topography, turbulent mixing is thought to be weak in the Southern Ocean interior (Ledwell et al. 2011). However, we find patches of relatively strong diffusivity throughout the water column (~10^{-3}–10^{-4} m^2 s^{-1}) and extending to 1400-m depth (Fig. 3). Here we analyze the role of bottom topography in the observed mixing variability.

The topographic roughness is estimated as the variance of the bottom height in a 0.1° × 0.1° box around each float location (Meyer et al. 2015). Changing the box size (resolutions of 0.05°, 0.15°, 0.2°) does not make any substantial change to the results (not shown). Mixing profiles were subsampled into regions of rough and smooth topography. Rough topography is defined as regions of roughness larger than the mean over all float profiles, 6.8×10^3 m^2, and smooth topography as regions with roughness smaller than the mean value. Changing this reference value does not change the results. Here, the mean roughness is smaller than that for the Kerguelen region (Meyer et al. 2015) and for the whole Southern Ocean (Wu et al. 2011), suggesting that the floats profiled over comparatively flat topography in between the steeper topography of the Southeast Indian Ridge upstream and Macquarie Ridge downstream. The mean water column depth over the float tracks is around 4000 m, reducing to about 3800 m over regions of rough topography.

Mean vertical profiles of dissipation rate and diffusivity over rough and smooth topography do not show a significant difference (Figs. 8a,b). If breaking of bottom-generated internal waves contributes to turbulent mixing in this region, we would expect to see a positive relationship between enhanced dissipation rate, bottom roughness, and bottom current speed with elevated mixing reaching 2000–3000 m above the sea floor (e.g., Garabato et al. 2004). If present, this topographic enhancement of dissipation might be evident in the deeper part of the float profiles. We test this by plotting dissipation and diffusivity averaged in the depth range 800–1400 m against a range of variables (Figs. 8c–f). We find no clear evidence of topographic enhancement of mixing in the float estimates (Fig. 8c). The dissipation rate estimates are smaller at this depth range compared to the shallow depths (Fig. 6). The diffusivity estimates are elevated at this depth range (Fig. 8d) due to a decrease in vertical stratification rather than an increase in dissipation rate with current speed and bottom roughness (Figs. 8a,b). In addition, we analyzed the dominant direction of propagation of the waves (Fig. 8e) and the corresponding frequency content (Fig. 8f) at the same depth range. The dissipation rate is slightly elevated for upward propagation (negative polarization ratio) at smaller values of roughness but decreases with an increase in roughness. Moreover, the elevated dissipation rate is associated with small roughness and near-inertial frequencies rather than higher-frequency waves. Overall, we do not observe a systematic elevation of dissipation rate associated with an increase in bottom roughness in the float mixing estimates. These analyses suggest that topography plays less role in mixing the upper water column in the study region. However, we cannot rule out the possibility of modification of bottom generated upward-propagating waves by the mesoscale eddy field. The lack of measurements below 1600 m restrict us from commenting on this any further.

6. Distribution of turbulent mixing

a. Mixing variability in different dynamic regimes

The floats encountered different dynamic regions such as fronts and mesoscale eddies during profiling. We did not see a direct correlation between elevated mixing and bottom

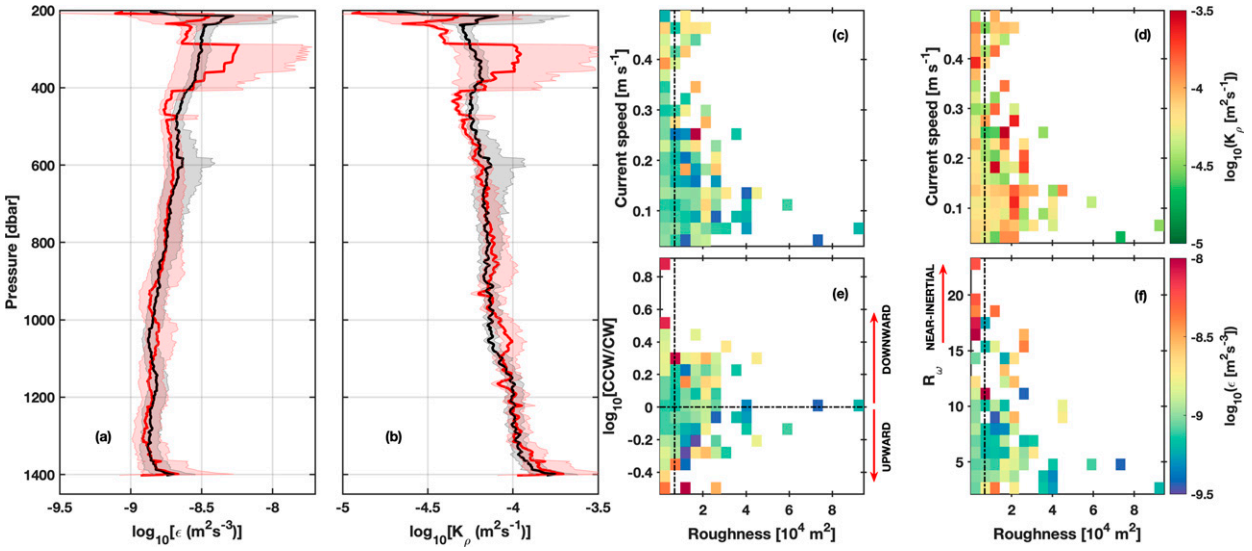

FIG. 8. Vertical profiles of mean (a) dissipation rate and (b) diffusivity over rough topography (red) and smooth topography (black). The sudden jump in dissipation rate and diffusivity in (a) and (b) is because the mixing values are only estimated below the mixed layer (section 2c, Fig. 3). Shaded areas show 90% confidence intervals estimated from bootstrap sampling. Mean (c) dissipation rate and (d) diffusivity averaged over 800–1400 m as a function of bottom roughness and current speed, (e) bottom roughness and polarization ratio, and (f) bottom roughness and R_ω. Note that (c) and (d) only take profiles from first half of the float tracks where we have current speeds (Fig. 2d). The vertical dashed line in all bin diagrams show the mean roughness (6.84×10^3 m^2) for the float data. The horizontal dashed line in (e) separates regions of upward energy propagation (negative values) and downward energy propagation (positive values).

roughness by comparing the whole float dataset (section 5c). Here, we investigate the role of different dynamic regions by subsampling the depth integrated dissipation rate in the upper 200–1200 m into regions of PF, SAF, and cyclonic and anticyclonic eddies and compare it with the corresponding bottom roughness (Fig. 9). The depth integrated dissipation rate in the upper water column (200–1200 m) ranges from 0.2 to 13.3 mW m^{-2} with a regional mean of 2 mW m^{-2} (Fig. 9a). The depth integrated dissipation rates lie in between the full water column dissipation values from microstructure (0.7–13.5 mW m^{-2}) north of Kerguelen Plateau (Waterman et al. 2013) and smaller than that inferred from finestructure parameterization with an assumption of $R_\omega = 3$ (10–20 mW m^{-2}) in the Drake Passage and Scotia Sea (Garabato et al. 2004). Figure 9a shows a large spread of depth integrated dissipation rate in all dynamic regions (0.2–13.3 mW m^{-2}) except in the PF (0.2–6 mW m^{-2}). However, we do not see a similar spread in the bottom roughness at the corresponding turbulent kinetic energy dissipation rate estimates along the float tracks (Fig. 9b). This suggests that the elevated depth averaged dissipation rates in different dynamic regions are less affected by bottom topography. Further, the averaged values of depth integrated dissipation rate and bottom roughness in different dynamic regions do not show a strong variability (Fig. 9c). The SAF (2.1 mW m^{-2}) and CE (2 mW m^{-2}) regions have similar depth integrated dissipation rates with PF (1.13 mW m^{-2}) having the smallest value. On the other hand, the mean bottom roughness over CE regions is the lowest (0.2×10^4 m^2) with highest roughness over the SAF region (1.2×10^4 m^2).

b. *Mixing and water masses*

Turbulent mixing plays an important role in the transformation of Southern Ocean water masses between different density classes. Figure 10 shows the mean profiles of dissipation rate and diffusivity on potential density levels to examine the variations in mixing in water mass layers. Mean profiles are presented for profiles in the PF, SAF, and in cyclonic and anticyclonic eddies. Dissipation rate and diffusivity are elevated in the AAIW layer in cyclonic eddy regions and weak in regions of anticyclonic eddies (Fig. 10) in agreement with a similar study in the Indian Ocean (Cyriac et al. 2021). However, in the SAMW layer, mixing is higher in anticyclonic eddies than in the cyclonic eddies. In the PF, diffusivity is weakest in the UCDW layer whereas the diffusivity in the SAF is the highest there (Fig. 10b). We observe weak diffusivity associated with SAMW whereas in regions of UCDW, the diffusivity is higher. Although there are distinct differences between different water masses and mixing, overall, these results indicate that the mesoscale eddies and ACC fronts equally contribute to the diapycnal mixing that drives water mass transformation in the upper water column in the Macquarie Ridge region.

7. Possible generation mechanisms

We showed in the previous sections that enhanced dissipation rate is associated with cyclonic vorticity and upward-propagating energy and is unrelated to the roughness of the local bathymetry. This evidence that strong currents over

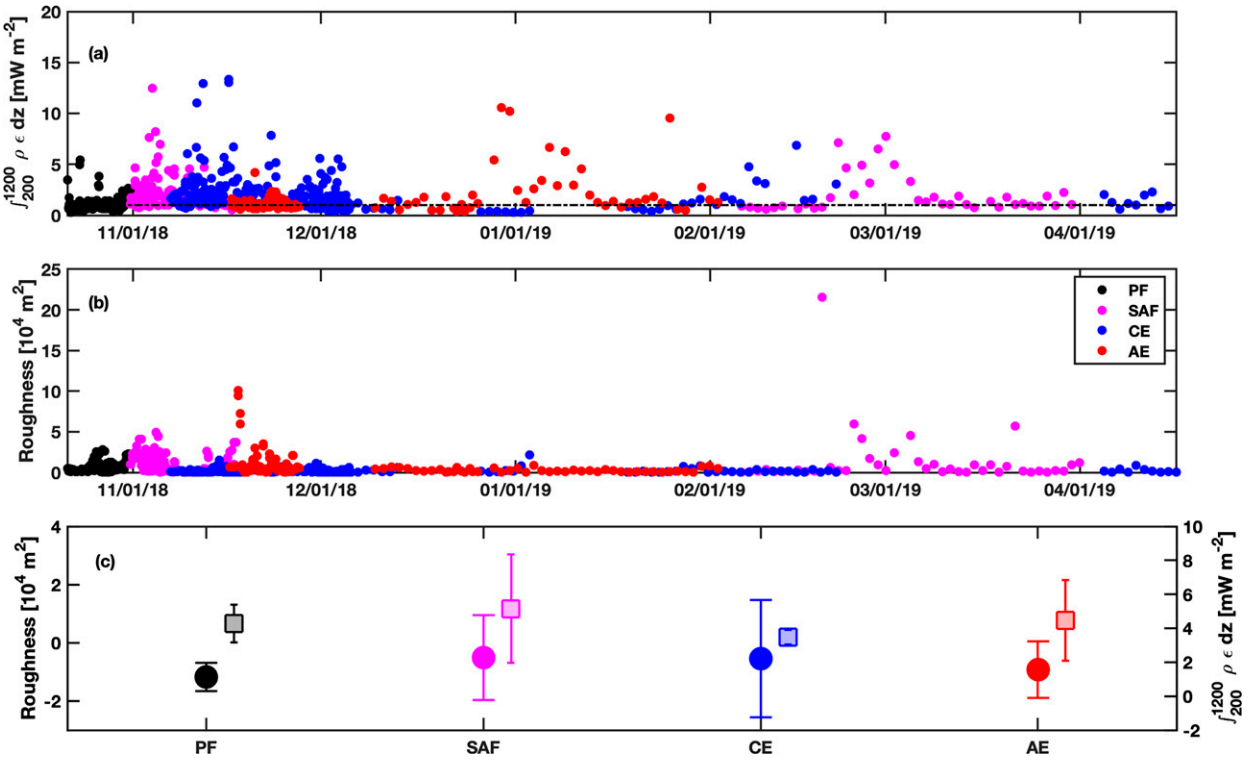

FIG. 9. (a) Depth-integrated dissipation rate and (b) topographic roughness along each float track as a function of time. (c) Bottom roughness values averaged over different dynamic regions (rectangles, left axis) and the averaged depth-integrated dissipation rate over the same regions (circles, right axis). The different dynamic regions considered here are the PF (black), SAF (magenta), CE (blue), and AE (red). The error bars represent one standard deviation of the variation of depth integrated dissipation rate (bottom roughness) for each dynamic region as shown in (a) and (b). Note the offset in x axis for both parameters for clarity.

rough bathymetry is not the mechanism by which near-inertial waves are generated here, leads us to explore alternate sources for the enhanced dissipation rate.

a. *Wind–eddy interactions*

The wind generated near-inertial waves play an important role in the spatial and temporal variability of turbulent mixing in the upper water column (Whalen et al. 2018). Previous studies have shown that the interaction between near-inertial waves and anticyclonic eddies is a major contributor to this mixing variability through different mechanisms such as near-inertial wave trapping when the relative vorticity of the eddy reduces the frequency of the internal waves to an effective frequency below f (e.g., Kunze 1985; Kunze et al. 1995), or near-inertial chimney where the wind-forced internal waves can be funneled to a critical layer at the eddy core (e.g., Lee and Niiler 1998), or wave capturing when the rate of strain exceeds the relative vorticity of the eddy (e.g., Bühler and McIntyre 2005; Polzin 2008).

Figure 11 shows depth-averaged diffusivity in two depth ranges (200–500 m and 500–1200 m) and for cyclonic and anticyclonic vorticity as a function of wind energy flux into inertial motions from the mixed layer slab model (section 5a). In the upper 250–500 m, there is no evidence of enhanced diffusivity in regions of anticyclonic vorticity with strong wind energy flux in contrast to the previous studies (Fig. 11). In addition, the mean diffusivity in cyclonic vorticity regions is higher than that in anticyclonic regions in this depth range. In the depth range of 500–1200 m, the mean diffusivity is similar for both cyclonic and anticyclonic vorticity regions and is larger than that in the upper layer irrespective of the sign of the vorticity. This indicates that the interaction between anticyclonic vorticity and near-inertial waves may be playing a less significant role in the observed turbulent mixing variability in this region.

b. *Tide–topography interactions*

One possible source for the upward-propagating energy are internal tides generated at the Macquarie Ridge (Waterhouse et al. 2018), a hotspot for M_2 tidal energy dissipation (Egbert and Ray 2000; Melet et al. 2014) mainly through barotropic tide–topography interactions. Both modeling studies (e.g., Simmons et al. 2004; Pinkel et al. 2015) and observations (Johnston et al. 2015) have shown that energetic M_2 baroclinic tides are generated at the ridge which then propagate northwestward into the Tasman Sea. Using altimetry data, Zhao et al. (2018) identified three internal tides generated at the ridge radiating into the Tasman Sea. They found that the southern beam with the second largest energy flux (0.7 GW) propagates into the strong ACC flow and disappears. These

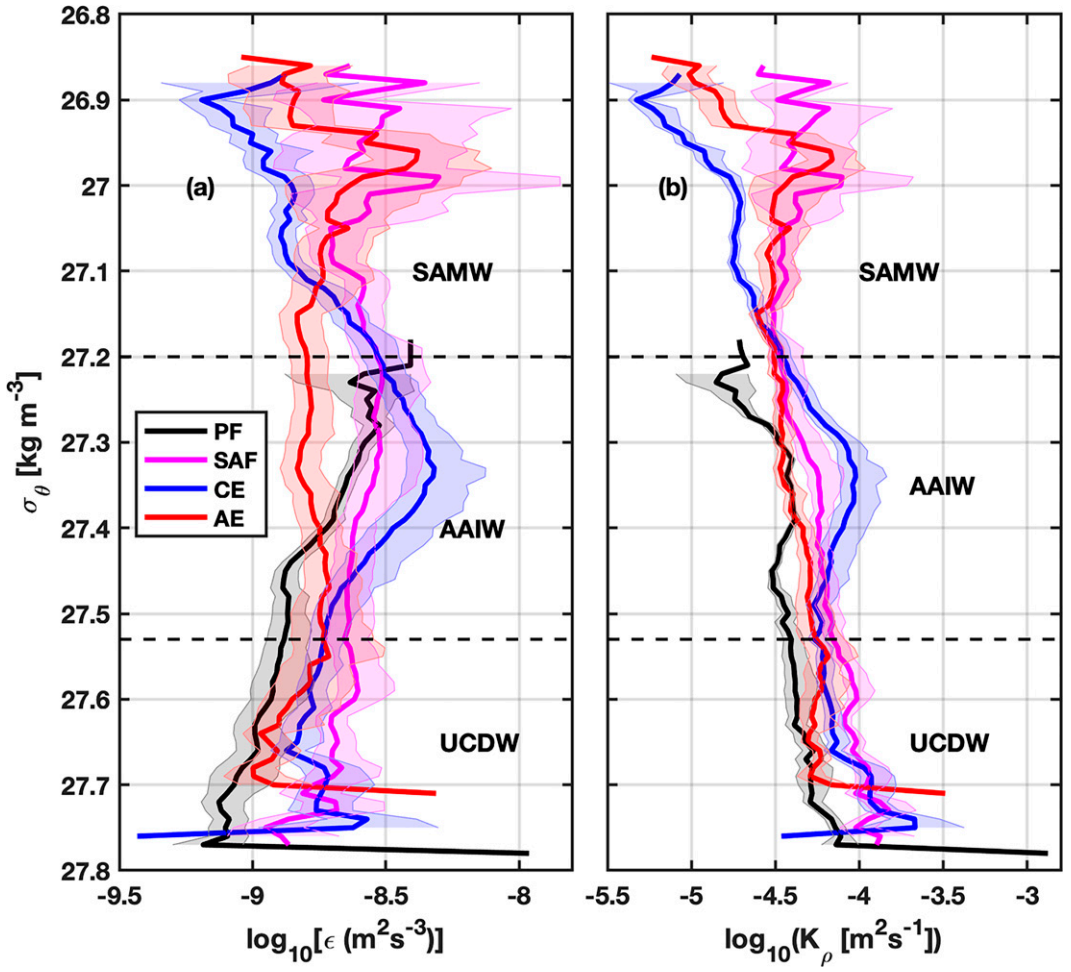

FIG. 10. Vertical profile of mean (a) dissipation rate and (b) diffusivity as a function of potential density (σ_θ) in PF (black), SAF (magenta), CE (blue), and AE (red). Different water masses are defined and marked as $\sigma_\theta \leq 27.2$ kg m^{-3} for SAMW, 27.2 kg m^{-3} $\leq \sigma_\theta \leq$ 27.53 kg m^{-3} for AAIW, and 27.53 kg m^{-3} $\leq \sigma_\theta \leq$ 27.8 kg m^{-3} for UCDW. Shaded areas show 90% confidence intervals estimated from bootstrap sampling.

internal tidal beams are also visible in the M_2 baroclinic tidal animations of the latest Multivariate Inversion of Ocean Surface Topography, Internal Tide Model (MIOST-IT) product from AVISO (https://www.aviso.altimetry.fr/en/index.php?id=5130). This product includes the M_2, S_2, O_1, and K_1 tidal frequencies on a 0.1° × 0.1° grid. Further, a velocity rotary spectrum from current meters deployed in the Macquarie Ridge gap at 53.45°S (Rintoul et al. 2014) shows dominant peaks at semidiurnal tidal frequencies (Fig. 12a) in agreement with global maps of tidal energy dissipation.

Generally, ocean currents contain subinertial, inertial, tidal, and high-frequency motions. To examine the relative strength of the semidiurnal tidal frequency in the region, we bandpass filtered the float velocities into these frequency ranges and estimated the corresponding depth integrated horizontal kinetic energy (HKE) over different depth ranges (Fig. 12b). Here we consider subinertial flow ($<0.98f$, where f is the mean Coriolis frequency of the float track), near-inertial waves ($0.98f$–$1.02f$, the inertial period at 53.6°S is 14.8 h), semidiurnal tides ($0.99M_2$–$1.25M_2$), and high-frequency waves ($>1.25M_2$). A narrow frequency range is taken for near-inertial waves and semidiurnal tides in order to avoid overlapping between the two (Fig. 12a). The subinertial HKE is highest in the upper 600 m as expected. In the deeper layers (600–1100 m), the semidiurnal tidal and high-frequency motions are the major contributors of HKE. Overall, the near-inertial energy is the lowest with highest energies in the superinertial frequencies.

Even though our data are insufficient to explicitly show that the upward-propagating energy is due to internal tides, the dominance of horizontal kinetic energy in the semidiurnal tidal frequency band (Fig. 12) and the circumstantial evidence from the above mentioned studies indicate that the upward energy could be due to internal tides generated at the ridge and propagated into the mesoscale field in the study region. The role of internal tide–mesoscale interactions will be

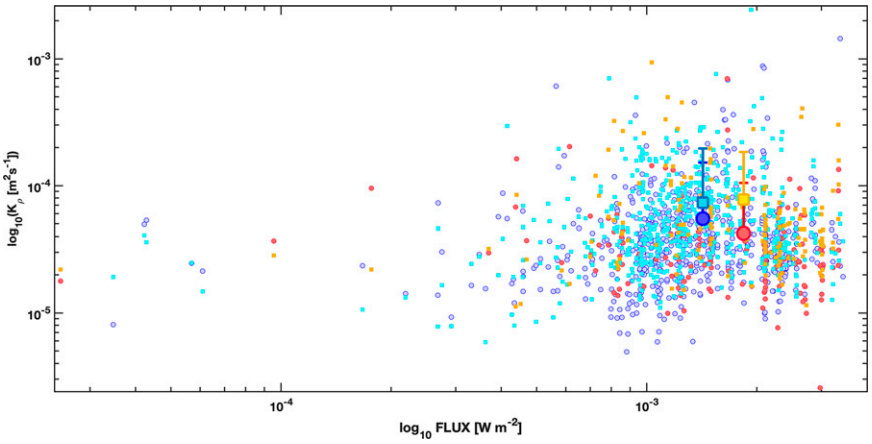

FIG. 11. Mean diffusivity averaged over 200–500 m (circles) as a function of wind energy flux into near-inertial motions along the float tracks over cyclonic (negative) vorticity regions (blue) and anticyclonic (positive) vorticity regions (red). The cyan (cyclonic) and yellow (anticyclonic) rectangles are the same for mean diffusivity over 500–1200 m. The all-profile means for both depth ranges are represented by the thick circles and rectangles, respectively. The error bars represent one standard deviation of the depth averaged diffusivity estimates for each vorticity regions at different depth ranges.

explored in a future study using the regional numerical model in Zhang and Nikurashin (2020).

c. *Current–topography interactions*

Another possible generation mechanism is the nonlocal dissipation of wave energy where upward-propagating, bottom-generated internal lee waves have become uncorrelated with the topography as they reach the upper ocean. This could be due to horizontal and vertical propagation of the waves, horizontal advection by the mean flow, temporal variability, or the orientation of the bottom flow relative to the topography (Waterman et al. 2013). The simulations of Zhang and Nikurashin (2020) in the Macquarie Ridge region identified internal lee waves generated by the bottom flow over rough small-scale topography in sections of vertical velocity. They found internal lee wave motions up to a few kilometers above the bottom on both sides of the ridge that propagate horizontally. However, their model does not include internal tides which could be an important source of internal wave energy in this region. The float data are not deep enough to examine the near-bottom signals in the context of linear internal lee wave theory. This will be explored further in a future study by applying finescale parameterization to shipboard CTD and LADCP data collected at the time of the EM-APEX deployments. We hypothesize that the internal lee waves play a role based on our expectation of bottom wave generation and dissipation in regions of relatively large topographic roughness and near-bottom mean flow (Nikurashin and Ferrari 2010). However, it is not always a reasonable expectation to have a quasi-stationary response associated with quasi-stationary flow over rough topography where bottom boundary layer processes become dominant (Polzin and McDougall 2021).

We suggest that the enhanced dissipation rates in the upper 200–1600 m could be primarily due to the interaction between mesoscale eddies and upward-propagating internal tides and/or internal lee waves generated elsewhere over rough topography and propagated into the study region. The enhanced mixing over regions of the SAF could be due to upward-propagating lee waves generated from the interactions between the front and the bottom bathymetry. Meyer et al. (2015) identified topographic roughness, wind, and current speed as the main factors contributing to the turbulent mixing variability in the upper 1600 m at the northern Kerguelen Plateau. They found traces of enhanced mixing at the edges of a cyclonic eddy. Moreover, Cyriac et al. (2021) found that the interactions between downward-propagating internal waves and mesoscale eddies are the major sources of turbulent mixing in the upper 1600 m of the eastern subtropical Indian Ocean, a region with unique circulation, weak internal tidal energy, and high eddy kinetic energy. These studies suggest that wave–mean flow interactions could be a major source of turbulent mixing variability in high eddy kinetic energy regions, as suggested both regionally using direct estimates (Polzin 2010; Cusack et al. 2020) and ray tracing (Waterman et al. 2021) and in similar global studies (Whalen et al. 2012, 2018).

8. Conclusions

We analyzed the spatial and temporal variability of diapycnal mixing in an energetic standing meander of the Southern Ocean between the southeast Indian Ridge and the Macquarie Ridge. The results point to a variety of possible mechanisms that contribute to the observed turbulent mixing variability:

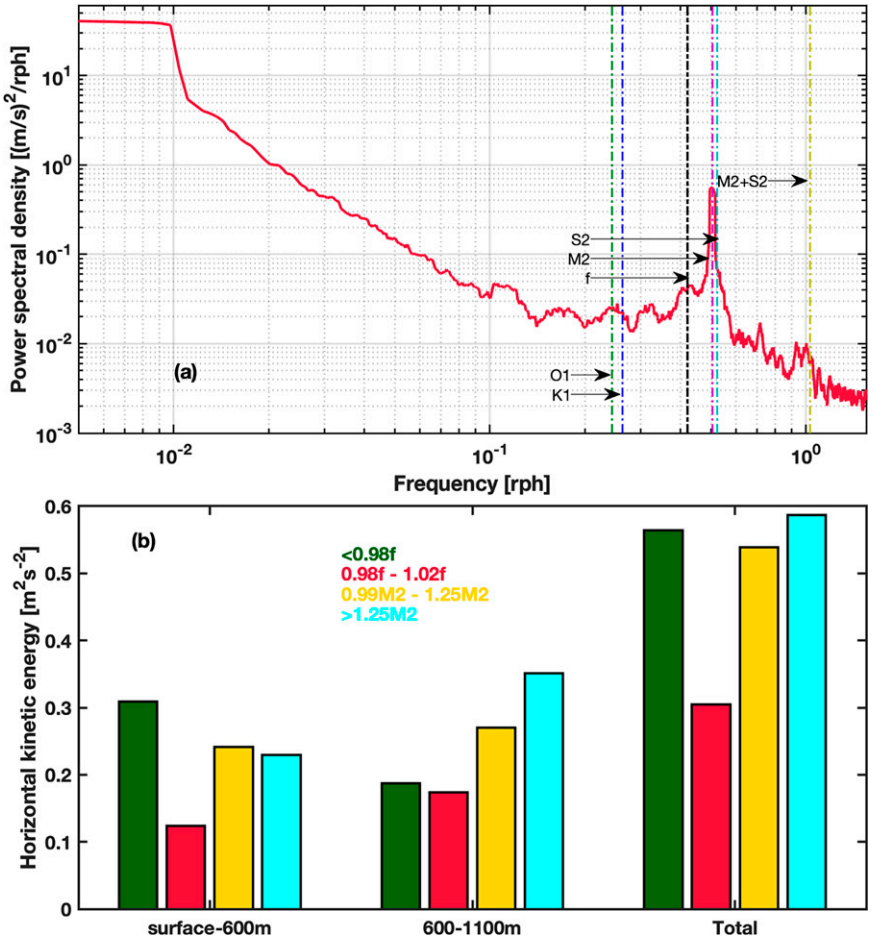

FIG. 12. (a) Velocity rotary spectrum from mooring velocities at the ridge gap at 53.45°S (Fig. 1c). (b) Depth integrated HKE at different frequency ranges [subinertial flow (<0.98*f*, where *f* is the mean Coriolis frequency of the float track), near-inertial waves (0.98*f*–1.02*f*, the inertial period at 53.6°S is 14.8 h), semidiurnal tides ($0.99M_2$–$1.25M_2$), and high-frequency waves (>$1.25M_2$)] from the float EM-8493.

- We find that downward-propagating wind-generated near-inertial waves are associated with elevated dissipation and turbulent mixing, suggesting a significant role for near-inertial waves in the variability of turbulent mixing.
- The interaction between cyclonic eddies and upward-propagating internal waves resulted in enhanced mixing in the upper 500 m of the water column.
- The most likely source of upward-propagating internal waves in cyclonic eddies is related to semidiurnal tidal generation. There is little evidence for lee waves providing a local source since there is no correlation between enhanced dissipation and local bottom roughness. Nonlocal lee wave generation and propagation of those waves cannot be ruled out.

The dissipation rate and turbulent mixing estimates from our EM-APEX data show strong spatial and temporal variability in the upper 1600 m of the Southern Ocean. The mixing is more intense within the SAF compared to the PF. Similarly, the mixing is higher in cyclonic eddies compared to anticyclonic eddies. The enhanced mixing in the cyclonic eddy regions is likely to cause greater water mass modifications, especially in the AAIW layer. The characteristics of the internal waves responsible for the observed mixing (and its variation) will be explored in a companion study which is currently under preparation.

Acknowledgments. We thank the scientists, student volunteers, and crew from the IN2018-V05 voyage on board the R/V *Investigator*. The observations were funded through grants from the Australian Research Council Discovery Project (DP170102162) and Australia's Marine National Facility. Surface drifters were provided by Dr. Shaun Dolk of the Global Drifter Program. AC was supported by an Australian Research Council Postdoctoral Fellowship. AC, HEP, and NLB acknowledge support from the Australian Government Department of the Environment and Energy National Environmental Science Program and the ARC Centre of

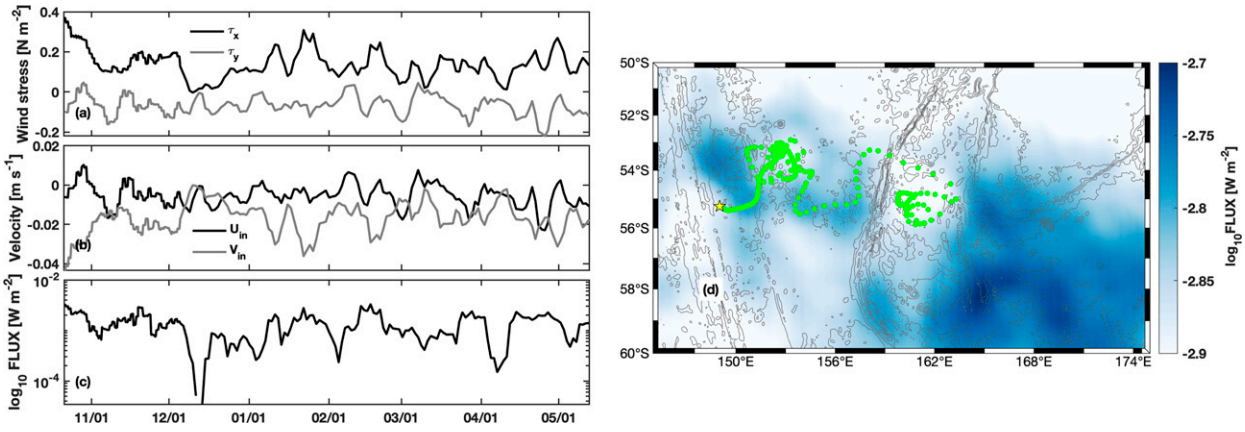

FIG. A1. Wind energy flux into near-inertial motions estimated using a mixed layer slab model. The (a) wind stress, (b) inertial currents from the slab model, and (c) wind energy flux along the track of EM-8493. (d) Mean wind energy flux over the study region from 13 Sep 2018 to 12 May 2019. The green circles show the track of float EM-8493. The gray contours are bathymetry as in Fig. 1.

Excellence in Climate Extremes. KP acknowledges the support from the National Science Foundation.

Data availability statement. The primary data used in this study are collected from three EM-APEX floats. These data are being prepared to be lodged and publicly available at the data repository of Institute for Marine and Antarctic Studies, University of Tasmania. Further details about the data quality control and processing are described in Cyriac et al. (2021). The other datasets are openly available at locations cited in section 2.

APPENDIX

Mixed Layer Slab Model of Wind Energy Flux

We ran the slab model (Pollard and Millard 1970) using ERA5 reanalysis winds with a constant mixed layer depth of 70 m (mean of the float data) and a damping constant of $0.15f$, where f is the mean Coriolis frequency along the float track. See Plueddemann and Farrar (2006) for a discussion about the choice of damping time scales. The wind energy flux into near-inertial motions is estimated as $\Pi = \tau U$, where τ ($\tau_x + i\tau_y$) is the wind stress and U ($u + iv$) is the mixed layer velocity estimated from the slab model (Silverthorne and Toole 2009; Alford 2003). This energy flux is then averaged over a period of 15–20 days prior to each mixing estimate from the float profiles to account for the time lag between near-inertial wave generation and their breaking at a deeper depth (Fig. A1).

REFERENCES

Alford, M. H., 2003: Improved global maps and 54-year history of wind-work on ocean inertial motions. *Geophys. Res. Lett.*, **30**, 1424–1429, https://doi.org/10.1029/2002GL016614.

——, and Z. Zhao, 2007: Global patterns of low-mode internal-wave propagation. Part I: Energy and energy flux. *J. Phys. Oceanogr.*, **37**, 1829–1848, https://doi.org/10.1175/JPO3085.1.

——, M. F. Cronin, and J. M. Klymak, 2012: Annual cycle and depth penetration of wind-generated near-inertial internal waves at ocean station papa in the northeast Pacific. *J. Phys. Oceanogr.*, **42**, 889–909, https://doi.org/10.1175/JPO-D-11-092.1.

——, J. A. MacKinnon, H. L. Simmons, and J. D. Nash, 2016: Near-inertial internal gravity waves in the ocean. *Annu. Rev. Mar. Sci.*, **8**, 95–123, https://doi.org/10.1146/annurev-marine-010814-015746.

Ansong, J. K., and Coauthors, 2017: Semidiurnal internal tide energy fluxes and their variability in a Global Ocean Model and moored observations. *J. Geophys. Res. Oceans*, **122**, 1882–1900, https://doi.org/10.1002/2016JC012184.

Böning, C. W., A. Dispert, M. Visbeck, S. Rintoul, and F. U. Schwarzkopf, 2008: The response of the Antarctic Circumpolar Current to recent climate change. *Nat. Geosci.*, **1**, 864–869, https://doi.org/10.1038/ngeo362.

Bray, N. A., and N. P. Fofonoff, 1981: Available potential-energy for MODE eddies. *J. Phys. Oceanogr.*, **11**, 30–47, https://doi.org/10.1175/1520-0485(1981)011<0030:APEFME>2.0.CO;2.

Bryden, H. L., and R. A. Heath, 1985: Energetic eddies at the northern edge of the Antarctic Circumpolar Current in the southwest Pacific. *Prog. Oceanogr.*, **14**, 65–87, https://doi.org/10.1016/0079-6611(85)90006-0.

Büuhler, O., and E. McIntyre, 2005: Wave capture and wave-vortex duality. *J. Fluid Mech.*, **534**, 67–95, https://doi.org/10.1017/S0022112005004374.

Chavanne, C., P. Flament, D. Luther, and K. Gurgel, 2010: The surface expression of semidiurnal internal tides near a strong source at Hawaii. Part II: Interactions with mesoscale currents. *J. Phys. Oceanogr.*, **40**, 1180–1200, https://doi.org/10.1175/2010JPO4223.1.

Cusack, J. M., J. A. Brearley, A. C. Naveira Garabato, D. A. Smeed, K. L. Polzin, N. Velzeboer, and C. J. Shakespeare, 2020: Observed eddy–internal wave interactions in the southern ocean. *J. Phys. Oceanogr.*, **50**, 3043–3062, https://doi.org/10.1175/JPO-D-20-0001.1.

Cyriac, A., H. E. Phillips, N. L. Bindoff, H. Mao, and M. Feng, 2021: Observational estimates of turbulent mixing in the southeast Indian Ocean. *J. Phys. Oceanogr.*, **51**, 2103–2128, https://doi.org/10.1175/JPO-D-20-0036.1.

de Boyer Montégut, C., G. Madec, A. S. Fischer, A. Lazar, and D. Iudicone, 2004: Mixed layer depth over the global ocean:

An examination of profile data and a profile-based climatology. *J. Geophys. Res.*, **109**, C12003, https://doi.org/10.1029/2004JC002378.

Dufour, C. O., A. K. Morrison, S. M. Griffies, I. Frenger, H. Zanowski, and M. Winton, 2017: Preconditioning of the Weddell Sea polynya by the ocean mesoscale and dense water overflows. *J. Climate*, **30**, 7719–7737, https://doi.org/10.1175/JCLI-D-16-0586.1.

Egbert, G. D., and R. D. Ray, 2000: Significant dissipation of tidal energy in the deep ocean inferred from satellite altimeter data. *Nature*, **405**, 775–778, https://doi.org/10.1038/35015531.

Foppert, A., K. A. Donohue, D. R. Watts, and K. L. Tracey, 2017: Eddy heat flux across the Antarctic Circumpolar Current estimated from sea surface height standard deviation. *J. Geophys. Res. Oceans*, **122**, 6947–6964, https://doi.org/10.1002/2017JC012837.

Frenger, I., M. Münnich, N. Gruber, and R. Knutti, 2015: Southern ocean eddy phenomenology. *J. Geophys. Res. Oceans*, **120**, 7413–7449, https://doi.org/10.1002/2015JC011047.

Garabato, A. C. N., K. L. Polzin, B. A. King, K. J. Heywood, and M. Visbeck, 2004: Widespread intense turbulent mixing in the southern ocean. *Science*, **303**, 210–213, https://doi.org/10.1126/science.1090929.

Gordon, A. L., 1975: An Antarctic oceanographic section along 170°E. *Deep-Sea Res. Oceanogr. Abstr.*, **22**, 357–377, https://doi.org/10.1016/0011-7471(75)90060-1.

——, 1978: On the interaction of the Antarctic Circumpolar Current and the Macquarie Ridge. *Antarct. Oceanol. II*, **19**, 71–78, https://doi.org/10.1029/AR019p0071.

Gregg, M. C., 1989: Scaling turbulent dissipation in the thermocline. *J. Geophys. Res.*, **94**, 9686–9698, https://doi.org/10.1029/JC094iC07p09686.

——, T. B. Sanford, and D. P. Winkel, 2003: Reduced mixing from the breaking of internal waves in equatorial waters. *Nature*, **422**, 513–515, https://doi.org/10.1038/nature01507.

——, E. A. D'Asaro, J. J. Riley, and E. Kunze, 2018: Mixing efficiency in the ocean. *Annu. Rev. Mar. Sci.*, **10**, 443–473, https://doi.org/10.1146/annurev-marine-121916-063643.

Hallberg, R., and A. Gnanadesikan, 2006: The role of eddies in determining the structure and response of the wind-driven Southern Hemisphere overturning: Results from the Modeling Eddies in the Southern Ocean (MESO) project. *J. Phys. Oceanogr.*, **36**, 2232–2252, https://doi.org/10.1175/JPO2980.1.

Henyey, F. S., J. Wright, and S. M. Flatte, 1986: Energy and action flow through the internal wave field: An eikonal approach. *J. Geophys. Res.*, **91**, 8487–8495, https://doi.org/10.1029/JC091iC07p08487.

Johnston, T. S., D. L. Rudnick, and S. M. Kelly, 2015: Standing internal tides in the Tasman Sea observed by gliders. *J. Phys. Oceanogr.*, **45**, 2715–2737, https://doi.org/10.1175/JPO-D-15-0038.1.

Kunze, E., 1985: Near-inertial wave-propagation in geostrophic shear. *J. Phys. Oceanogr.*, **15**, 544–565, https://doi.org/10.1175/1520-0485(1985)015<0544:NIWPIG>2.0.CO;2.

——, R. W. Schmitt, and J. M. Toole, 1995: The energy balance in a warm-core ring's near-inertial critical layer. *J. Phys. Oceanogr.*, **25**, 942–957, https://doi.org/10.1175/1520-0485(1995)025<0942:TEBIAW>2.0.CO;2.

Ledwell, J. R., L. C. St. Laurent, J. B. Girton, and J. M. Toole, 2011: Diapycnal mixing in the Antarctic Circumpolar Current. *J. Phys. Oceanogr.*, **41**, 241–246, https://doi.org/10.1175/2010JPO4557.1.

Lee, D. K., and P. P. Niiler, 1998: The inertial chimney: The near-inertial energy drainage from the ocean surface to the deep layer. *J. Geophys. Res.*, **103**, 7579–7591, https://doi.org/10.1029/97JC03200.

Marshall, D. P., M. H. Ambaum, J. R. Maddison, D. R. Munday, and L. Novak, 2017: Eddy saturation and frictional control of the Antarctic Circumpolar Current. *Geophys. Res. Lett.*, **44**, 286–292, https://doi.org/10.1002/2016GL071702.

Melet, A., R. Hallberg, S. Legg, and M. Nikurashin, 2014: Sensitivity of the ocean state to lee wave–driven mixing. *J. Phys. Oceanogr.*, **44**, 900–921, https://doi.org/10.1175/JPO-D-13-072.1.

Meyer, A., B. M. Sloyan, K. L. Polzin, H. E. Phillips, and N. L. Bindoff, 2015: Mixing variability in the southern ocean. *J. Phys. Oceanogr.*, **45**, 966–987, https://doi.org/10.1175/JPO-D-14-0110.1.

——, K. L. Polzin, B. M. Sloyan, and H. E. Phillips, 2016: Internal waves and mixing near the Kerguelen Plateau. *J. Phys. Oceanogr.*, **46**, 417–437, https://doi.org/10.1175/JPO-D-15-0055.1.

Morozov, E. G., 1995: Semidiurnal internal wave global field. *Deep-Sea Res. I*, **42**, 135–148, https://doi.org/10.1016/0967-0637(95)92886-C.

Nadeau, L.-P., and R. Ferrari, 2015: The role of closed gyres in setting the zonal transport of the Antarctic Circumpolar Current. *J. Phys. Oceanogr.*, **45**, 1491–1509, https://doi.org/10.1175/JPO-D-14-0173.1.

Nikurashin, M., and R. Ferrari, 2010: Radiation and dissipation of internal waves generated by geostrophic motions impinging on small-scale topography: Theory. *J. Phys. Oceanogr.*, **40**, 1055–1074, https://doi.org/10.1175/2009JPO4199.1.

——, G. K. Vallis, and A. Adcroft, 2013: Routes to energy dissipation for geostrophic flows in the southern ocean. *Nat. Geosci.*, **6**, 48–51, https://doi.org/10.1038/ngeo1657.

Orsi, A. H., T. Whitworth III, and W. D. Nowlin Jr., 1995: On the meridional extent and fronts of the Antarctic Circumpolar Current. *Deep-Sea Res. I*, **42**, 641–673, https://doi.org/10.1016/0967-0637(95)00021-W.

Osborn, T., 1980: Estimates of the local rate of vertical diffusion from dissipation measurements. *J. Phys. Oceanogr.*, **10**, 83–89, https://doi.org/10.1175/1520-0485(1980)010<0083:EOTLRO>2.0.CO;2.

Patel, R. S., H. E. Phillips, P. G. Strutton, A. Lenton, and J. Llort, 2019: Meridional heat and salt transport across the Subantarctic Front by cold-core eddies. *J. Geophys. Res. Oceans*, **124**, 981–1004, https://doi.org/10.1029/2018JC014655.

Phillips, H. E., and S. R. Rintoul, 2000: Eddy variability and energetics from direct current measurements in the Antarctic Circumpolar Current south of Australia. *J. Phys. Oceanogr.*, **30**, 3050–3076, https://doi.org/10.1175/1520-0485(2000)030<3050:EVAEFD>2.0.CO;2.

——, and N. Bindoff, 2014: On the nonequivalent barotropic structure of the Antarctic Circumpolar Current: An observational perspective. *J. Geophys. Res. Oceans*, **119**, 5221–5243, https://doi.org/10.1002/2013JC009516.

Pinkel, R., M. Alford, A. Lucas, S. Johnston, J. MacKinnon, A. Waterhouse, and P. Strutton, 2015: Breaking internal tides keep the ocean in balance. *Eos*, **96**, https://doi.org/10.1029/2015EO039555.

Plueddemann, A., and J. Farrar, 2006: Observations and models of the energy flux from the wind to mixed-layer inertial currents. *Deep-Sea Res. II*, **53**, 5–30, https://doi.org/10.1016/j.dsr2.2005.10.017.

Pollard, R. T., and R. Millard, 1970: Comparison between observed and simulated wind-generated inertial oscillations.

Deep-Sea Res. Oceanogr. Abstr., **17**, 813–821, https://doi.org/10.1016/0011-7471(70)90043-4.

Polzin, K. L., 2008: Mesoscale eddy-internal wave coupling. Part I: Symmetry, wave capture, and results from the mid-ocean dynamics experiment. *J. Phys. Oceanogr.*, **38**, 2556–2574, https://doi.org/10.1175/2008JPO3666.1.

——, 2010: Mesoscale eddy–internal wave coupling. Part II: Energetics and results from polymode. *J. Phys. Oceanogr.*, **40**, 789–801, https://doi.org/10.1175/2009JPO4039.1.

——, and T. J. McDougall, 2021: Mixing at the ocean's bottom boundary. *Ocean Mixing*, M. M. Meredith and A. C. N. Garabato, Eds., Elsevier, 145–180.

——, J. M. Toole, and R. W. Schmitt, 1995: Finescale parameterizations of turbulent dissipation. *J. Phys. Oceanogr.*, **25**, 306–328, https://doi.org/10.1175/1520-0485(1995)025<0306:FPOTD>2.0.CO;2.

——, J. Toole, J. Ledwell, and R. Schmitt, 1997: Spatial variability of turbulent mixing in the abyssal ocean. *Science*, **276**, 93–96, https://doi.org/10.1126/science.276.5309.93.

——, E. Kunze, J. Hummon, and E. Firing, 2002: The finescale response of lowered ADCP velocity profiles. *J. Atmos. Oceanic Technol.*, **19**, 205–224, https://doi.org/10.1175/1520-0426(2002)019<0205:TFROLA>2.0.CO;2.

——, A. C. N. Garabato, T. N. Huussen, B. M. Sloyan, and S. Waterman, 2014: Finescale parameterizations of turbulent dissipation. *J. Geophys. Res. Oceans*, **119**, 1383–1419, https://doi.org/10.1002/2013JC008979.

Rintoul, S. R., 2018: The global influence of localized dynamics in the southern ocean. *Nature*, **558**, 209–218, https://doi.org/10.1038/s41586-018-0182-3.

——, S. Sokolov, M. Williams, B. Peña Molino, M. Rosenberg, and N. Bindoff, 2014: Antarctic Circumpolar Current transport and barotropic transition at Macquarie Ridge. *Geophys. Res. Lett.*, **41**, 7254–7261, https://doi.org/10.1002/2014GL061880.

Roemmich, D., S. Riser, R. Davis, and Y. Desaubies, 2004: Autonomous profiling floats: Workhorse for broad-scale ocean observations. *Mar. Technol. Soc. J.*, **38**, 21–29, https://doi.org/10.4031/002533204787522802.

Sanford, T. B., J. H. Dunlap, J. A. Carlson, D. C. Webb, and J. B. Girton, 2005: Autonomous velocity and density profiler: EM-APEX. *Proc. IEEE/OES Eighth Working Conf. on Current Measurement Technology*, Southampton, United Kingdom, Institute of Electrical and Electronics Engineers, 152–156, https://doi.org/10.1109/CCM.2005.1506361.

Sheen, K., and Coauthors, 2013: Rates and mechanisms of turbulent dissipation and mixing in the southern ocean: Results from the Diapycnal and Isopycnal Mixing Experiment in the Southern Ocean (DIMES). *J. Geophys. Res. Oceans*, **118**, 2774–2792, https://doi.org/10.1002/jgrc.20217.

Silverthorne, K. E., and J. M. Toole, 2009: Seasonal kinetic energy variability of near-inertial motions. *J. Phys. Oceanogr.*, **39**, 1035–1049, https://doi.org/10.1175/2008JPO3920.1.

Simmons, H. L., R. W. Hallberg, and B. K. Arbic, 2004: Internal wave generation in a global baroclinic tide model. *Deep-Sea Res. II*, **51**, 3043–3068, https://doi.org/10.1016/j.dsr2.2004.09.015.

Sloyan, B. M., 2005: Spatial variability of mixing in the Southern Ocean. *Geophys. Res. Lett.*, **32**, L18603, https://doi.org/10.1029/2005GL023568.

Sokolov, S., and S. R. Rintoul, 2002: Structure of southern ocean fronts at 140°E. *J. Mar. Syst.*, **37**, 151–184, https://doi.org/10.1016/S0924-7963(02)00200-2.

——, and ——, 2007: Multiple jets of the Antarctic Circumpolar Current south of Australia. *J. Phys. Oceanogr.*, **37**, 1394–1412, https://doi.org/10.1175/JPO3111.1.

——, and ——, 2009: Circumpolar structure and distribution of the Antarctic Circumpolar Current fronts: 2. Variability and relationship to sea surface height. *J. Geophys. Res.*, **114**, C11019, https://doi.org/10.1029/2008JC005248.

Straub, D. N., 1993: On the transport and angular momentum balance of channel models of the Antarctic Circumpolar Current. *J. Phys. Oceanogr.*, **23**, 776–782, https://doi.org/10.1175/1520-0485(1993)023<0776:OTTAAM>2.0.CO;2.

Tamsitt, V., and Coauthors, 2017: Spiraling pathways of global deep waters to the surface of the southern ocean. *Nat. Commun.*, **8**, 172, https://doi.org/10.1038/s41467-017-00197-0.

Thompson, A. F., and A. C. Naveira Garabato, 2014: Equilibration of the Antarctic Circumpolar Current by standing meanders. *J. Phys. Oceanogr.*, **44**, 1811–1828, https://doi.org/10.1175/JPO-D-13-0163.1.

Vanneste, J., 2013: Balance and spontaneous wave generation in geophysical flows. *Annu. Rev. Fluid Mech.*, **45**, 147–172, https://doi.org/10.1146/annurev-fluid-011212-140730.

Waterhouse, A. F., and Coauthors, 2018: Observations of the Tasman Sea internal tide beam. *J. Phys. Oceanogr.*, **48**, 1283–1297, https://doi.org/10.1175/JPO-D-17-0116.1.

Waterman, S., A. C. N. Garabato, and K. L. Polzin, 2013: Internal waves and turbulence in the Antarctic Circumpolar Current. *J. Phys. Oceanogr.*, **43**, 259–282, https://doi.org/10.1175/JPO-D-11-0194.1.

——, A. Meyer, K. L. Polzin, A. C. Naveira Garabato, and K. L. Sheen, 2021: Antarctic Circumpolar Current impacts on internal wave life cycles. *Geophys. Res. Lett.*, **48**, e2020GL089471, https://doi.org/10.1029/2020GL089471.

Whalen, C. B., L. D. Talley, and J. A. MacKinnon, 2012: Spatial and temporal variability of global ocean mixing inferred from Argo profiles. *Geophys. Res. Lett.*, **39**, L18612, https://doi.org/10.1029/2012GL053196.

——, J. A. MacKinnon, and L. D. Talley, 2018: Large-scale impacts of the mesoscale environment on mixing from wind-driven internal waves. *Nat. Geosci.*, **11**, 842–847, https://doi.org/10.1038/s41561-018-0213-6.

Wilson, C., C. W. Hughes, and J. R. Blundell, 2015: Forced and intrinsic variability in the response to increased wind stress of an idealized southern ocean. *J. Geophys. Res. Oceans*, **120**, 113–130, https://doi.org/10.1002/2014JC010315.

Wu, L., Z. Jing, S. Riser, and M. Visbeck, 2011: Seasonal and spatial variations of southern ocean diapycnal mixing from Argo profiling floats. *Nat. Geosci.*, **4**, 363–366, https://doi.org/10.1038/ngeo1156.

Wunsch, C., and R. Ferrari, 2004: Vertical mixing, energy, and the general circulation of the oceans. *Annu. Rev. Fluid Mech.*, **36**, 281–314, https://doi.org/10.1146/annurev.fluid.36.050802.122121.

Zhang, X., and M. Nikurashin, 2020: Small-scale topographic form stress and local dynamics of the Southern Ocean. *J. Geophys. Res. Oceans*, **125**, e2019JC015420, https://doi.org/10.1029/2019JC015420.

Zhao, Z., M. H. Alford, H. L. Simmons, D. Brazhnikov, and R. Pinkel, 2018: Satellite investigation of the M_2 internal tide in the Tasman Sea. *J. Phys. Oceanogr.*, **48**, 687–703, https://doi.org/10.1175/JPO-D-17-0047.1.